Necl-1/CADM3 regulates cone synapse formation in the mouse retina

Kawashima, Rumi ; Matsushita, Kenji ; Mandai, Kenji ; Sugita, Yuko ; Maruo, Tomohiko ; Mizutani, Kiyohito ; Midoh, Yoshihiro ; Oguchi, Akik…

(Citation)
iScience,27(4):109577

(Issue Date)
2024-04-19

(Resource Type)
journal article

(Version)
Version of Record

iScience

CellPress
OPEN ACCESS

Article

Necl-1/CADM3 regulates cone synapse formation in the mouse retina

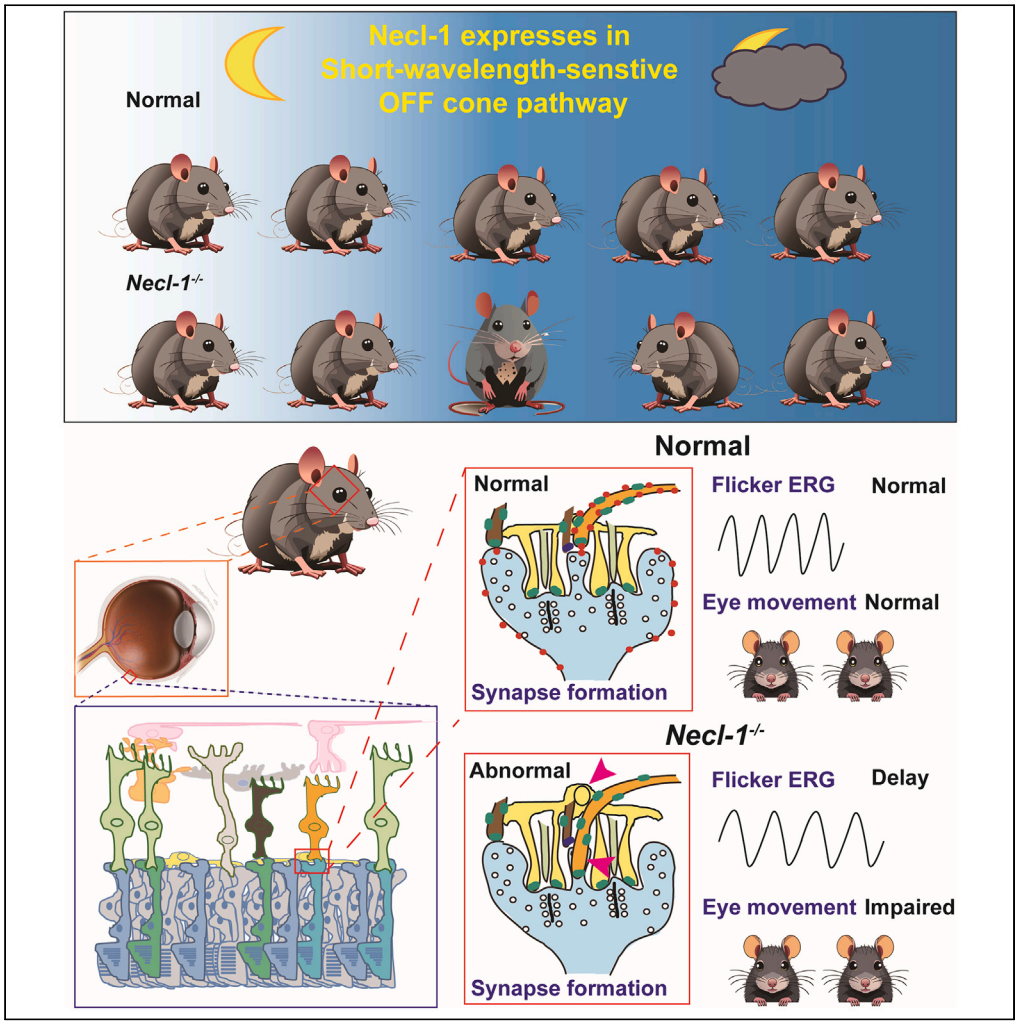

Rumi Kawashima, Kenji Matsushita, Kenji Mandai, ..., Takahisa Furukawa, Kohji Nishida, Yoshimi Takai

kenmatsu@ophthal.med.osaka-u.ac.jp (K.M.)
ytakai@med.kobe-u.ac.jp (Y.T.)

Highlights

Necl-1 is essential for correct cone synapse location

Necl-1 regulates short-wavelength-light-sensitive OFF cone pathways

Necl-1 is required for normal visual function in mouse retina

Kawashima et al., iScience 27, 109577
April 19, 2024
https://doi.org/10.1016/j.isci.2024.109577

iScience

CellPress
OPEN ACCESS

Article

Necl-1/CADM3 regulates cone synapse formation in the mouse retina

Rumi Kawashima,[1] Kenji Matsushita,[1,11,*] Kenji Mandai,[2,3,4] Yuko Sugita,[5] Tomohiko Maruo,[2,3] Kiyohito Mizutani,[2,6] Yoshihiro Midoh,[9] Akiko Oguchi,[7] Yasuhiro Murakawa,[7] Kazuki Kuniyoshi,[8] Ryohei Sato,[10] Takahisa Furukawa,[5] Kohji Nishida,[1] and Yoshimi Takai[2,*]

SUMMARY

In vertebrates, retinal neural circuitry for visual perception is organized in specific layers. The outer plexiform layer is the first synaptic region in the visual pathway, where photoreceptor synaptic terminals connect with bipolar and horizontal cell processes. However, molecular mechanisms underlying cone synapse formation to mediate OFF pathways remain unknown. This study reveals that Necl-1/CADM3 is localized at S- and S/M-opsin-containing cones and dendrites of type 4 OFF cone bipolar cells (CBCs). In *Necl-1*$^{-/-}$ mouse retina, synapses between cones and type 4 OFF CBCs were dislocated, horizontal cell distribution became abnormal, and α-amino-3-hydroxy-5-methyl-4-isoxazolepropionic acid (AMPA) receptors were dislocated. *Necl-1*$^{-/-}$ mice exhibited aberrant short-wavelength-light-elicited signal transmission from cones to OFF CBCs, which was rescued by AMPA receptor potentiator. Additionally, *Necl-1*$^{-/-}$ mice showed impaired optokinetic responses. These findings suggest that Necl-1 regulates cone synapse formation to mediate OFF cone pathways elicited by short-wavelength light in mouse retina.

INTRODUCTION

In vertebrate retina, rod and cone photoreceptor cells (rods and cones) mediate the initial step of vision. The human retina contains three types of cones: short-wavelength cones (S-cones or blue cones), middle-wavelength cones (M-cones or green cones), and long-wavelength cones (L-cones or red cones). In contrast, mouse retina contains three types of cones: S-opsin-containing, M-opsin-containing, and S/M-opsin-containing cones (Figure 1A).[1,2] Visual signals detected by these cones and rods are processed through parallel ON and OFF pathways in the retinal circuitry.[3,4] Segregation of ON and OFF pathways begins with ON bipolar cells (BCs) and OFF BCs (Figures 1A and 1B).[5] A cone photoreceptor terminus makes contacts with multiple ON bipolar termini in invaginated pits and with multiple OFF bipolar termini with flat ends on cones. An invaginated rod photoreceptor terminus makes contact with a single rod BC (ON) terminus (Figure 1A). Cone BCs (CBCs), consisting of ON and OFF CBCs, receive signal inputs predominantly from cones, while rod BCs consist of only one type, ON BCs. ON BCs express metabotropic glutamate receptor 6 (mGluR6 encoded by the *Grm6* gene) on their dendrites,[6] whereas OFF CBCs express ionotropic GluRs (α-amino-3-hydroxy-5-methyl-4-isoxazolepropionic acid (AMPA)/kainate (KA) receptors) and glutamate-gated cation channels on their dendrites.[7] In the dark, glutamate is released at a high rate from photoreceptor cell terminals, and this released glutamate depolarizes OFF CBCs via ionotropic GluRs and hyperpolarizes ON BCs through mGluR6 activation to close TRPM1 cation channels (Figure 1B).[8]

Photoreceptor cells contact ON BCs and horizontal cells (HCs) through specialized synapses called ribbon synapses (Figures 1A and 1B). HCs are inhibitory interneurons that build large receptive fields by electrically coupling via gap junctions. HCs are activated by glutamate released from photoreceptor cells and provide feedback and feedforward signals to photoreceptor cells and BCs, respectively[9,10] as well as auto-feedback signals to HCs.[11] An HC ablation mouse study showed that HCs are required for generating physiological subtype diversity of retinal ganglion cells (RGCs), adjustment of sensitivity to ambient light at the retinal output level, and spatial frequency tuning at the organismal level, suggesting multiple functional roles of HCs that are pivotal for visual processing.[12] HCs contact cone photoreceptor synaptic terminals and send feedback signals to cones, which may be important in color vision by generating color opponent interactions.[13] However,

[1]Department of Ophthalmology, Osaka University Graduate School of Medicine, Suita, Osaka 565-0871, Japan
[2]Division of Pathogenetic Signaling, Department of Biochemistry and Molecular Biology, Kobe University Graduate School of Medicine, Kobe, Hyogo 650-0047, Japan
[3]Department of Molecular and Cellular Neurobiology, Kitasato University Graduate School of Medical Sciences, Sagamihara, Kanagawa 252-0374, Japan
[4]Department of Biochemistry, Kitasato University School of Medicine, Sagamihara, Kanagawa 252-0374, Japan
[5]Laboratory for Molecular and Developmental Biology, Institute for Protein Research, Osaka University, Suita, Osaka 565-0871, Japan
[6]Division of Pathogenetic Signaling, Institute of Advanced Medical Sciences, Tokushima University, Tokushima 770-8503, Japan
[7]RIKEN-IFOM Joint Laboratory for Cancer Genomics, IMS RIKEN Center for Integrative Medical Sciences, Yokohama, Kanagawa 230-0045, Japan
[8]Department of Ophthalmology, Kindai University Faculty of Medicine, Osakasayama, Osaka 589-8511, Japan
[9]Graduate School of Information Science and Technology, Osaka University, Suita, Osaka 565-0871, Japan
[10]Forefront Research Center for Graduate School of Science, Osaka University, Toyonaka, Osaka 560-0043, Japan
[11]Lead contact
*Correspondence: kenmatsu@ophthal.med.osaka-u.ac.jp (K.M.), ytakai@med.kobe-u.ac.jp (Y.T.)
https://doi.org/10.1016/j.isci.2024.109577

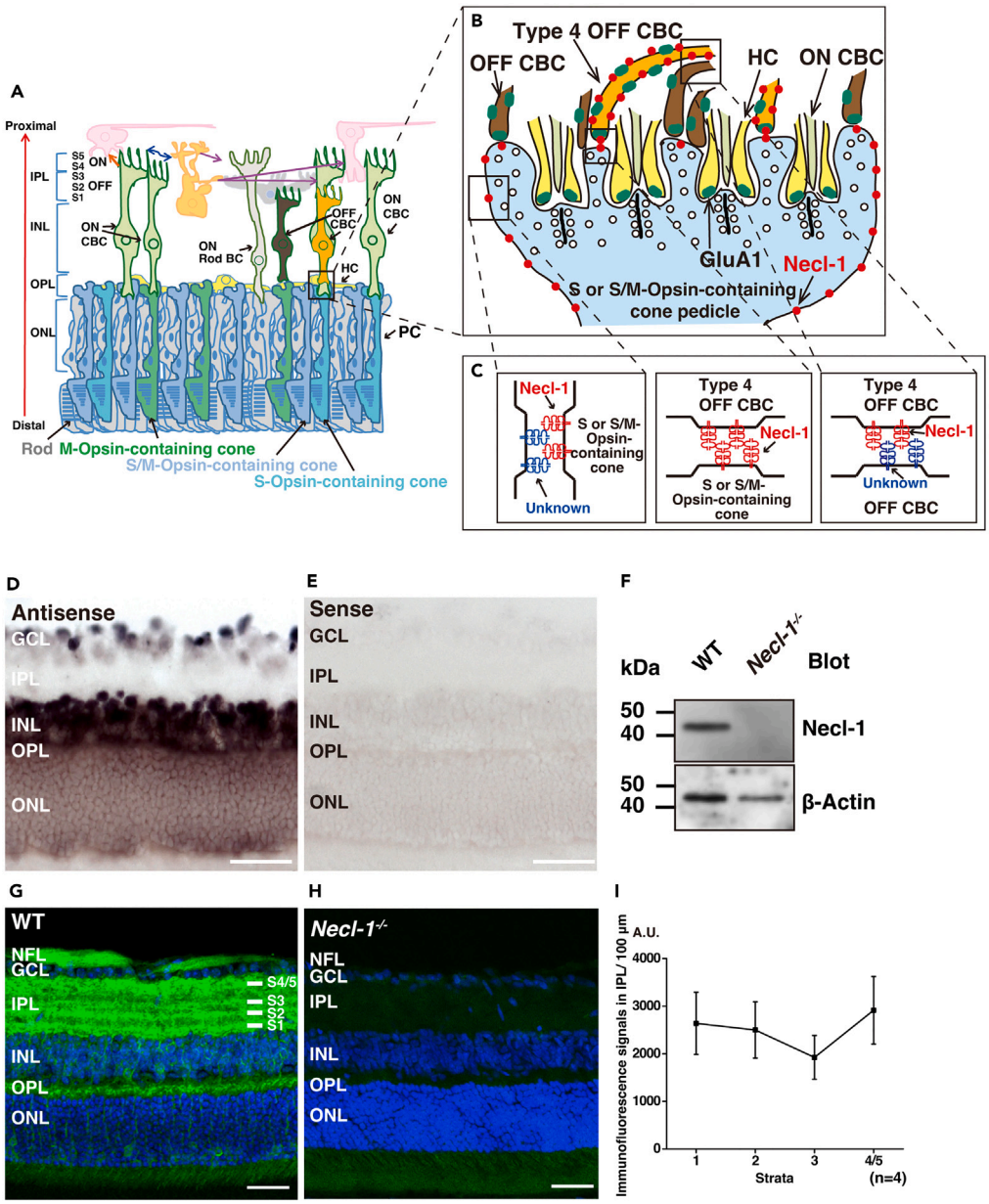

Figure 1. Necl-1 is abundantly expressed in mouse retina

Retinas from 8-week WT mice were stained with an anti-Necl-1 pAb, which recognizes the intracellular region of Necl-1 protein.

(A–C) Schematic drawings of an adult mouse retina and Necl-1 localization. (A) Transverse sectional view of the retina. Light pink, retinal ganglion cells; light orange, AII BCs; light gray, amacrine cells. Orange, dark blue, and magenta arrows show signal transduction between cells. (B) Transverse sectional view of an S or S/M-opsin-containing cone pedicle and the dense plexus near the basal synapse in WT mouse retina. Expression of Necl-1 is shown in red. White circles, synaptic vesicles; light yellow, HCs; light green, ON CBCs; orange, type 4 OFF CBCs; brown, OFF CBCs; and green oval, GluA1. (C) Schematic showing Necl-1-mediated cell adhesion at the cone pedicle (left and middle) and the dense plexus near basal synapses (right). (D and E) *In situ* hybridization for *Necl-1*.

(D) Antisense probe; (E) sense probe.

(F) Expression of Necl-1 in mouse retina. Lysates obtained from 8-week WT and *Necl-1*$^{-/-}$ mouse retinas were subjected to western blotting using an anti-Necl-1 pAb and an anti-β-actin pAb.

(G and H) Immunohistochemistry in *Necl-1*$^{-/-}$ mouse retina. Retinas of 8-week WT and *Necl-1*$^{-/-}$ mice from the same litter were subjected to immunohistochemistry using the anti-Necl-1 pAb. (I) Quantification of the Necl-1 signal detected in each stratum of the IPL. NFL, nerve fiber layer; GCL, ganglion cell layer; IPL, inner plexiform layer; INL, inner nuclear layer; OPL, outer plexiform layer; ONL, outer nuclear layer; and PC, photoreceptor cell. Scale bars in D, E, G, and H, 20 μm. Error bars in I represent ±SD from WT mouse (n = 4). See also Figure S1.

precise functional roles and mechanisms of HCs in color vision remain ambiguous. It is crucial to determine mechanisms of function and development of HCs in retinal circuits.

A variety of cell adhesion molecules (CAMs) have been identified as key components of retinal circuits and synapses.[14–19] Nectins and nectin-like molecules (Necls), which are also cell adhesion molecules (CADMs), comprise a family belonging to the immunoglobulin superfamily and serve as CAMs in the central nervous system.[20,21] Single-cell RNA-profiling analysis showed that *Necl-1/CADM3* and *Necl-2/CADM1* are abundantly expressed in BCs in mouse retina.[22] Necl-2 is associated with connections between rods and BCs in the outer plexiform layer (OPL).[23] *Necl-1/CADM3* mRNA is expressed in RGCs and in the inner nuclear layer (INL) in mouse retina[24] and *Necl-1/CADM3* is expressed strongly in photoreceptor cells and BCs in zebrafish retina[25]; however, the role of *Necl-1* in mouse retina is largely unknown.

Here, we show that Necl-1 is localized on dendrites of type 4 OFF CBCs in the OPL and at the plasma membrane near synaptic terminals of S-and S/M-opsin-containing cones in mouse retina. We also show that Necl-1 regulates synapse formation between OFF CBCs and S- or S/M-opsin-containing cones to mediate OFF cone pathways elicited by short-wavelength light.

RESULTS

Necl-1 is abundantly expressed in mouse retina

Necl-1 serves an important function in cell adhesion between nerve cells and glial cells and is required for myelination in the vertebrate central nervous system.[24,26] However, the role of Necl-1 in unmyelinated retinal neuronal cells remains unclear. To investigate the physiological role of Necl-1 in the retina, Necl-1 localization was first examined in 8-week-old (8-week) mouse retinas by immunostaining using an anti-Necl-1 polyclonal antibody (pAb) that we previously established.[24] Single-cell RNA profiling analysis showed that *Necl-1* mRNA is abundantly expressed in amacrine cells (ACs), OFF CBCs (BC1A-BC4), ON CBC (BC8/9), and cone photoreceptors in mouse retina (Figure S1A). *In situ* hybridization detected *Necl-1* mRNA in some RGCs, in outer nuclear layer (ONL) cells, and in inner nuclear layer cells (Figures 1D and 1E). We generated *Necl-1*$^{-/-}$ mice by targeted gene disruption (Figure S1B). *Necl-1*$^{-/-}$ mice were born at the expected Mendelian ratio (data not shown), and both *Necl-1*$^{+/-}$ and *Necl-1*$^{-/-}$ mice were viable and showed no gross morphological abnormalities. Western blot analysis using an anti-Necl-1 Ab demonstrated the loss of a protein band with a molecular mass of 48 kD in *Necl-1*$^{-/-}$ mouse retina (Figure 1F). In addition, the Necl-1 immunofluorescence signal was observed in wild-type (WT) mouse retina, but not in *Necl-1*$^{-/-}$ mouse retina, using the anti-Necl-1 Ab, confirming the high specificity of this Ab against the Necl-1 protein (Figures 1G and 1H). The Necl-1 immunofluorescence signal was highly concentrated in S1 and S2 sublaminae (OFF sublayers) and the S4/S5 sublamina (ON sublayer) of the inner plexiform layer (IPL) and the OPL (Figures 1G and 1I). The Necl-1 signal was also observed in some cells in the inner nuclear layer and the outer nuclear layer. In the ONL, the Necl-1 signal was concentrated in somata of cells in the outermost layer of the ONL and on axons of these cells (Figure 1G).

Necl-1 is expressed in retinal cone photoreceptor cells

While Necl-1 localization in the IPL was previously reported in zebrafish and mouse retinas,[24,25] Necl-1 localization in the outer retina has not been reported. Thus, in the present study, we investigated localization and function of Necl-1 in mouse outer retina.

To identify which cell types express Necl-1 in the ONL, 8-week mouse retinal sections were double-immunostained using the anti-Necl-1 Ab with cell-type-specific marker Abs against CtBP2 (a marker for cones somata), S-opsin (a marker for S-opsin-positive cones), M-opsin (a marker for M-opsin-positive cones), and rhodopsin (a marker for rods) (Figures 2A–2D). The Necl-1 signal surrounding cone somata (Figure 2A) was detected at S-opsin-positive cone inner segments (Figure 2B) and in some M-opsin-positive cone inner segments (Figure 2C) but was not colocalized with the rhodopsin signal (Figure 2D). We analyzed the percentage of Necl-1-positive cells among the various photoreceptor cells. Necl-1 is expressed in S-opsin-positive cones and about half of M-opsin-positive cones but not in rods (Figure 2E). These results indicate that Necl-1 is localized at cone photoreceptor axons, perisomata, and inner segments, especially S-opsin-positive cones (Videos S1 and S2).

Necl-1 is expressed in OFF cone bipolar cells

Next, we examined whether Necl-1 is expressed in BCs. 8-week mouse retinal sections were double-immunostained using the anti-Necl-1 Ab with a cell-type-specific marker Ab against HCN4 (a marker for type 3a OFF CBCs), PKARIIβ (a marker for type 3b OFF CBCs), calsenilin (a marker for type 4 OFF CBCs), Syt2 (a marker for type 2 OFF and 6 ON CBCs), or PKCα (a marker for rod ON BCs) (Figures 3A–3E). The Necl-1 signal was hardly observed in somata or dendrites of Syt2-positive CBCs or PKCα-positive rod BCs (Figures 3D and 3E). The Necl-1 signal was observed in somata of some HCN4-positive type 3a OFF CBCs and PKARIIβ-positive type 3b OFF CBCs but not at their dendrites (Figures 3A and 3B). The Necl-1 signal was observed in somata and dendrites of all calsenilin-positive type 4 OFF CBCs (Figure 3C). 79.6 ± 6.4% of Necl-1-positive cells were Chx10-positive (n = 4; WT mouse), indicating that most Necl-1-positive cells were BCs. Hence, other Necl-1-positive cells observed in the INL might be ACs. Collectively, these results indicate that Necl-1 is localized only on somata of some type 3a and 3b, and on both somata and dendrites of all 4 OFF CBCs. We counted the number of Nec-1-surrounded Chx-10-positive BCs in the dorsal and ventral retina, respectively, using whole-mount immunostaining (Figure S2). These results showed that Necl-1-positive bipolar cells are more abundantly distributed in the ventral retina (Figure S2C).

Necl-1 is required for correct localization of synapses between cones and type 4 OFF CBCs

We next investigated the function of Necl-1 in formation and/or maintenance of synapses between cones and type 4 OFF CBCs using *Necl-1*$^{-/-}$ mice. Histological analyses of 8-week mouse retina showed no differences in cell density of S-opsin-positive cones (Figures 4A

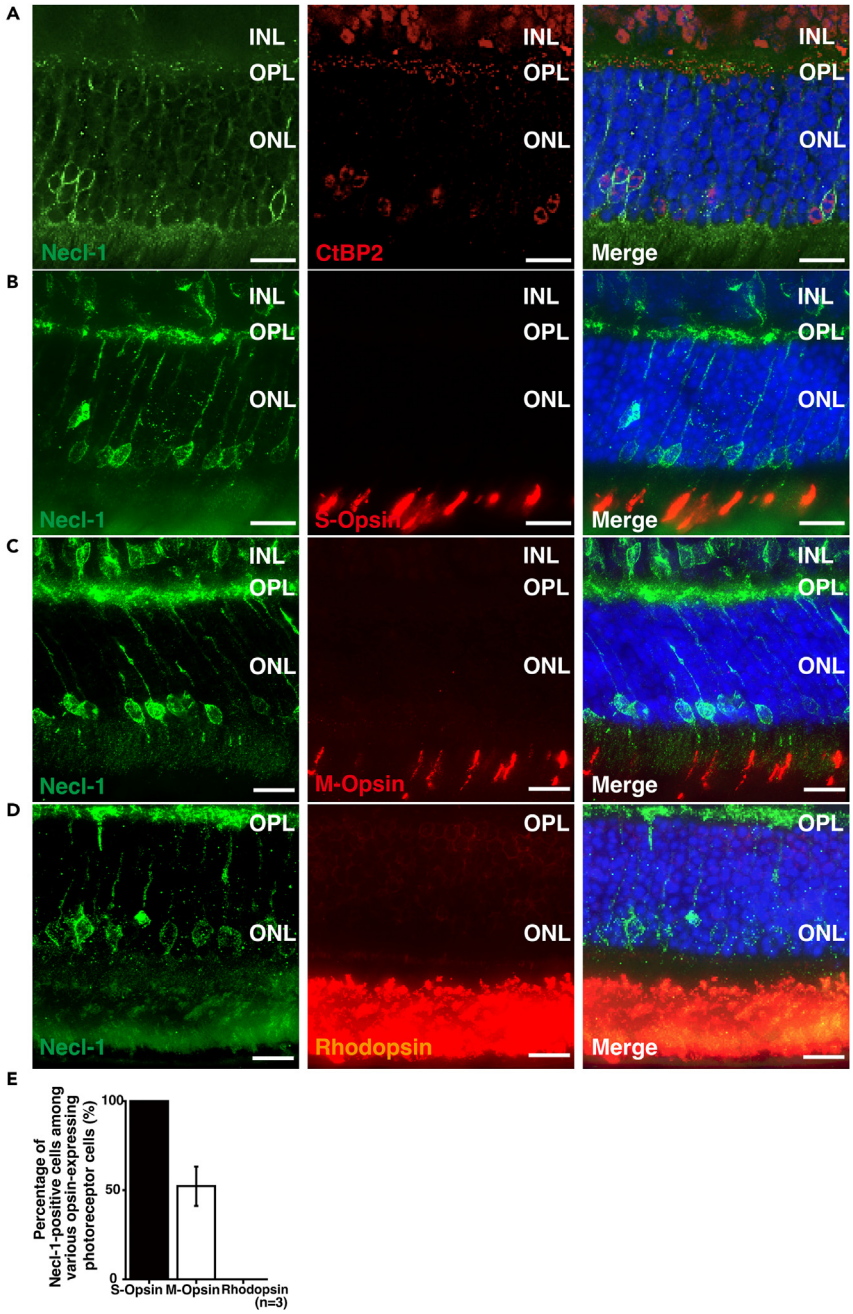

Figure 2. Necl-1 is expressed in retinal cone photoreceptor cells

(A–D) Localization of the Necl-1 signal in the OPL and ONL. The retina was double-immunostained with the Necl-1 pAb (green) plus one of the following Abs for various retinal photoreceptor cell marker proteins (red): (A) an anti-cone somata mAb (a marker for cones); (B) an anti-S-opsin pAb (a marker for S-opsin-positive cones); (C) an anti-*M*-opsin pAb (a marker for M-opsin-positive cones); (D) an anti-rhodopsin mAb (a marker for rods); (E) Observed percentage of Necl-1-positive cells among various opsin-expressing photoreceptor cells. INL, inner nuclear layer; OPL, outer plexiform layer; and ONL, outer nuclear layer. Scale bars in A–D, 15 μm. Error bars in E represent ±SD from means of n = 6 to 8 retina sections per WT mouse (n = 3).

and 4B; $p = 0.71$, paired Student's t test), bipolar cells (Figures 4C and 4D; p = 0.50, paired Student's t test), HCN4-positive type 3a OFF CBCs (Figures 4E and 4F; $p = 0.84$, paired Student's t test), PKARIIβ-positive type 3b OFF CBCs (Figures 4H and 4I; $p = 0.97$, paired Student's t test), or type 4 OFF CBCs (Figure 4K and 4L; $p = 0.59$, paired Student's t test) between wild-type (WT) and *Necl-1*$^{-/-}$ mice. Then, we analyzed dendritic extensions of type 3a, 3b, and 4 OFF CBCs, in which Necl-1 is localized. HCN, PKARIIβ, and calsenilin signals in *Necl-1*$^{-/-}$ mouse retina were examined by double-staining using an antibody against OFF CBC markers (anti-HCN, PKARIIβ, and calsenilin mAb) and a cone synapse

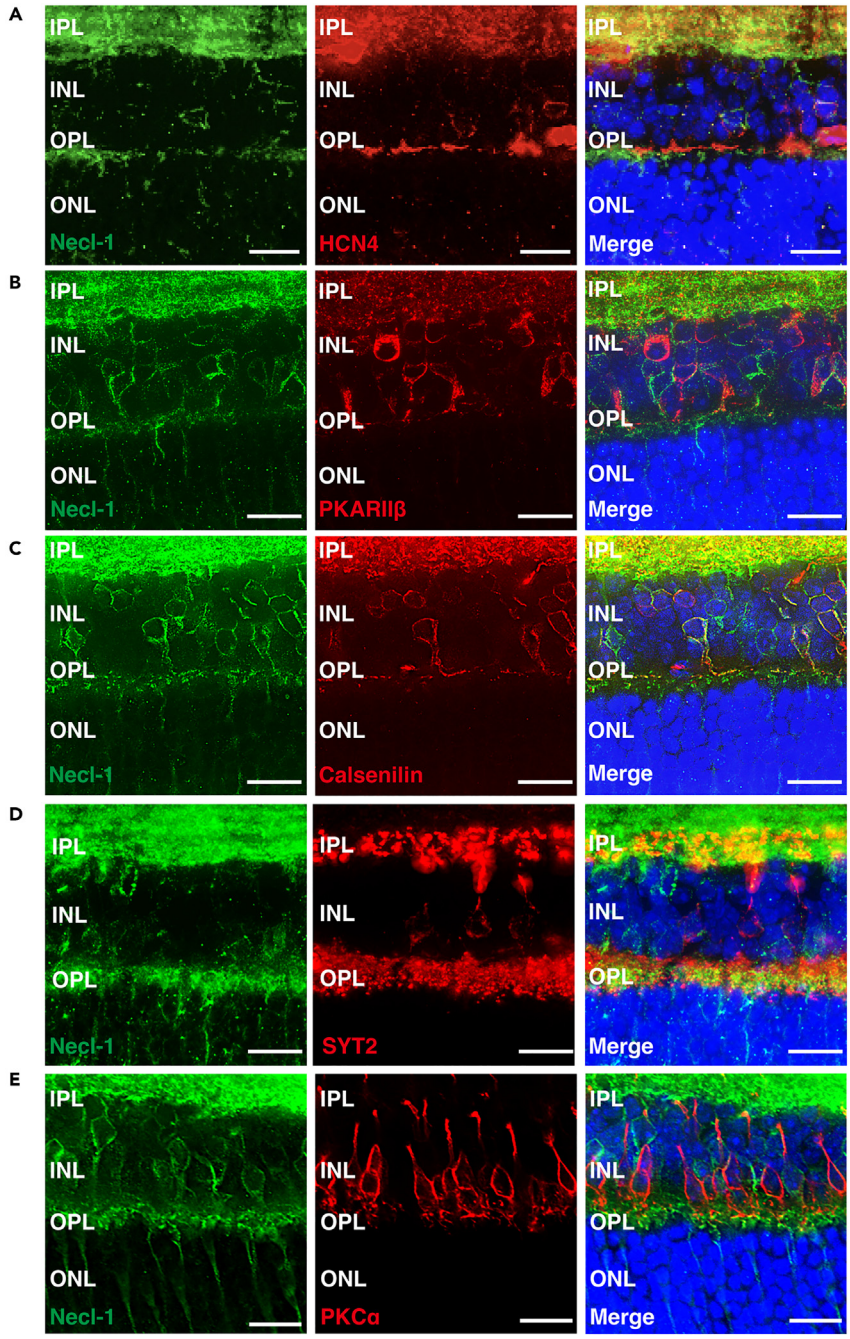

Figure 3. Necl-1 is expressed in OFF cone bipolar cells

(A–E) Localization of the Necl-1 signal in the INL, OPL, and ONL. The retina was double-immunostained with the Necl-1 pAb (green) plus one of the following Abs for various retinal bipolar cell marker proteins (red): (A) an anti-HCN4 mAb for type 3a OFF CBCs; (B) an anti-PKARIIβ mAb for type 3b OFF CBCs; (C) an anti-calsenilin mAb for type 4 OFF CBCs; (D) an anti-SYT2 mAb for type 2 OFF CBCs and 6 ON CBCs; (E) an anti-PKCα mAb for rod BCs. For nuclear counter staining (blue), 4′,6-diamidino-2-phenylindole (DAPI) was used. IPL, inner plexiform layer; INL, inner nuclear layer; OPL, outer plexiform layer; and ONL, outer nuclear layer. Scale bars in A–E, 15 μm. See also Figure S2.

marker, peanut agglutinin (PNA). We did not detect any differences in dendritic extensions from type 3a and 3b CBCs (Figures 4G and 4J), but excessive type 4 CBC dendrites extended into the outer retinal side compared to those in WT mouse retina. (Figures 4K and 4M; **, $p = 0.001$, paired Student's t test). The lack of effect on those BCs by Necl-1 ablation supports our claim that Necl-1 expression is enriched in type 4 OFF CBCs. Necl-1 expression was analyzed by immunostaining using the anti-Necl-1 Ab in developing WT mouse retinas at P2, P7, P14, and P21

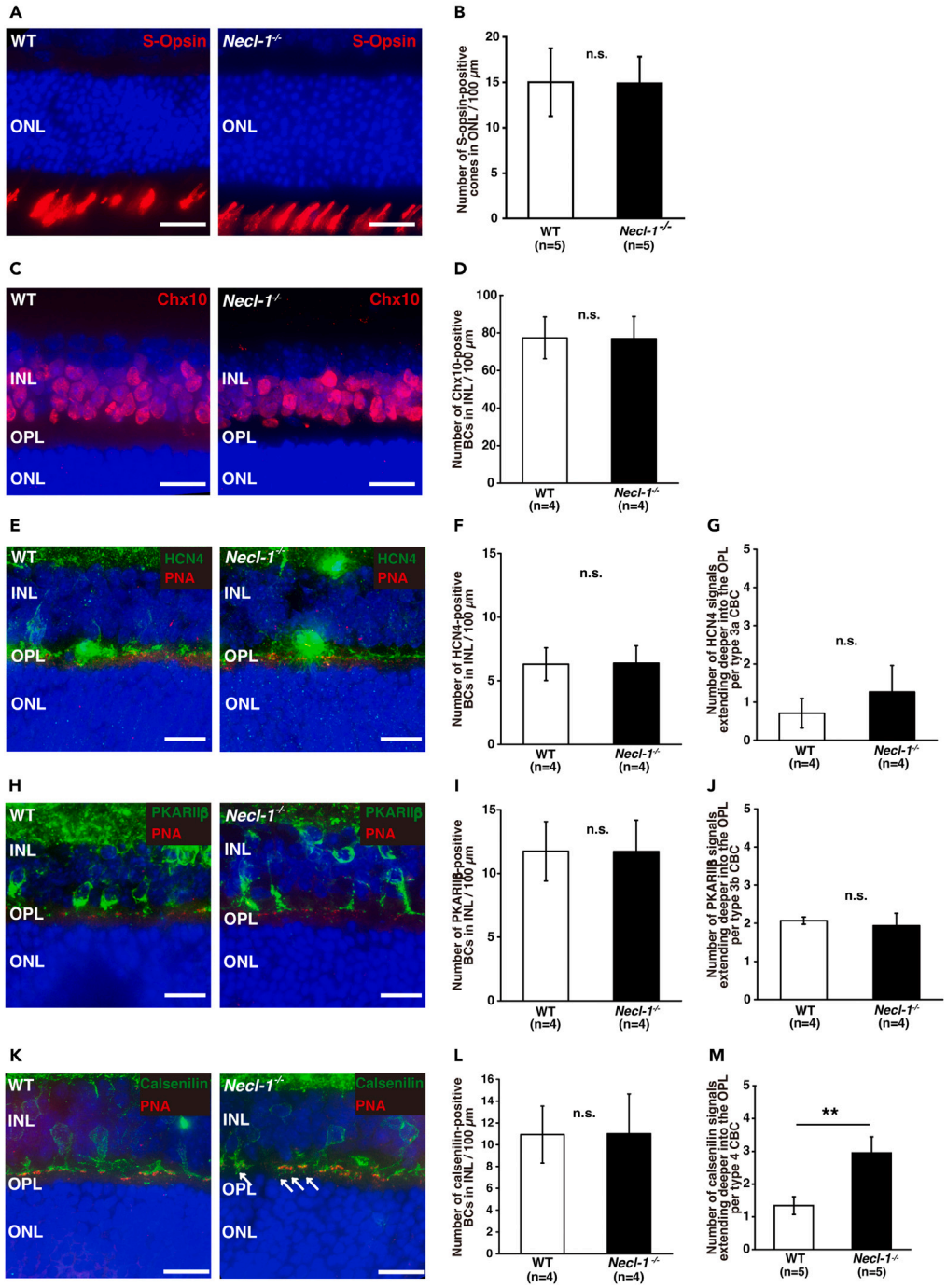

Figure 4. Role of Necl-1 in formation of synapses between cones and type 4 OFF CBCs

Retinas from 8-week WT and *Necl-1*$^{-/-}$ mice were used. (A and B) Density of S-opsin-positive cones.

(A) S-opsin-positive cones in the ONL. Red, S-opsin; and blue, DAPI. Scale bars, 15 μm.

(B) Density of S-opsin-positive cones. The average density of S-opsin-positive cones was calculated. Error bars represent ±SD from means of n = 7 to 9 retina sections collected from individual animals (n = 5; WT and *Necl-1*$^{-/-}$, respectively). n.s., not significant (p = 0.71) by paired Student's t test. (C and D) Density of bipolar cells.

(C) Bipolar cells in the ONL. Red, Chx10; and blue, DAPI. Scale bars, 15 μm.

(D) Density of bipolar cells. The average density of Chx10-positive cells was calculated. Error bars represent ±SD from means of n = 5 to 7 retina sections collected from individual animals (n = 4; WT and *Necl-1*$^{-/-}$, respectively). n.s., not significant (p = 0.50) by paired Student's t test.

Figure 4. *Continued*

(E–M) Density and abnormal extension of dendrites of OFF CBCs. (E, H, and K) Retinal sections stained with OFF CBC markers and peanut agglutinin (PNA). Green, HCN4 (E), PKARIIβ (H), and calsenilin (K); red, PNA; and blue, DAPI. Arrows indicate abnormal dendrites of type 4 OFF CBCs to the photoreceptor cell side in *Necl-1*$^{-/-}$mouse retina. Scale bars, 15 μm.

(F, I, and L) Average density of OFF CBCs was calculated. F, HCN4; I, PKARIIβ; L, calsenilin. Error bars represent ±SD from means of n = 5 to 8 retina sections collected from individual animals (n = 4; WT and *Necl-1*$^{-/-}$, respectively). n.s., not significant (F, p = 0.84; I, p = 0.97; L, p = 0.92) by paired Student's t test.

(G, J, and M) Number of dendrites of OFF CBCs extending into the ONL per OFF CBC. G, HCN4; J, PKARIIβ; M, calsenilin. Error bars represent ±SD from means of n = 5 to 8 retina sections collected from individual animals (n = 4 or 5; WT and *Necl-1*$^{-/-}$, respectively). n.s., not significant (G, p = 0.06; J, p = 0.44). **, p = 0.001 by paired Student's t test. See also Figure S3.

(Figure S3). Necl-1 was expressed in the OPL from P7, consistent with the previous observation that flat cone synapses make contacts with CBCs around P6 in mouse retina.[27] Collectively, these results indicate that Necl-1 is required for correct localization of synapses between cones and type 4 OFF CBCs.

Necl-1 is essential for proper signal transduction from short-wavelength-sensitive cones to OFF CBCs

To determine the physiological role of Necl-1 *in vivo*, electroretinograms (ERGs) of *Necl-1*$^{-/-}$ mice were measured under dark-adapted (scotopic) and light-adapted (photopic) conditions. Under scotopic conditions, amplitudes of a-waves and b-waves, originating mainly from activity of rod photoreceptor cells (a-waves) and of rod BCs (b-waves), did not differ significantly different between WT and *Necl-1*$^{-/-}$ mouse retinas (Figures S4A and S4B). Implicit times of scotopic a-waves and b-waves showed no significant change in *Necl-1*$^{-/-}$ mouse retina compared to WT mouse retina (Figure S4C). The amplitude and implicit time of oscillatory potential (OP) waves showed no significant change in *Necl-1*$^{-/-}$ mouse retina compared to those in WT mouse retina (Figures S4D–S4F). Much like scotopic ERGs, amplitudes of photopic a-waves and b-waves, mainly reflecting population activity of cone photoreceptor cells (a-waves) and cone ON BCs (b-waves), were comparable between WT and *Necl-1*$^{-/-}$ mouse retinas (Figures S5A–S5C). These results suggest that *Necl-1* deficiency does not affect cone photoreceptor or cone ON BC functions. Next, photopic flicker ERGs were measured to examine OFF pathway activation in the M-opsin-mediated signaling pathway using the white light-emitting diode (LED)-stimulated ERG recording system established previously.[28] Those photopic flicker ERGs showed that amplitudes and implicit times did not differ significantly between WT and *Necl-1*$^{-/-}$ mouse retinas (Figures S5D–S5F).

Since a white LED flash stimulates mainly the M-opsin ~510-nm peak but barely the S-opsin ~360-nm peak (Figure S6), we measured photopic flicker ERGs to examine OFF pathway activation in the S-opsin-mediated signaling pathway using an ultraviolet (UV) LED, 360-nm-stimulated ERG recording system, established previously to isolate S-opsin-mediated signals[29] (see also the details in STAR Methods) (Figure 5A). In photopic flicker ERGs of *Necl-1*$^{-/-}$ mice, amplitudes of photopic flicker ERGs did not differ significantly between WT and *Necl-1*$^{-/-}$ mouse retinas (Figure 5B). However, peak times, induced by UV LED stimulation at 25 and 30 Hz, were delayed significantly compared to those of WT mouse retina (Figure 5C; *, p = 0.03 and **, p = 0.002, paired Student's t test). Thus, the peak time delay of high frequency flicker ERGs in *Necl-1*$^{-/-}$ mouse retina may be associated with synaptic dysfunction in the OFF pathway in the OPL. In addition, to observe OFF pathway activities, the ON pathway was eliminated by injecting WT and *Necl-1*$^{-/-}$ mice with L-2-amino-4-phosphonobutyric acid (L-AP4) and performing long-duration flash ERGs (Figures 5D–5F).[30] The amplitude for *Necl-1*$^{-/-}$ mouse retina was smaller than that for WT mouse retina, but this difference was not statistically significant (Figure 5E). Implicit times from trough to peak of *Necl-1*$^{-/-}$ mice were significantly more delayed at 100 and 150 ms compared to those of WT mouse retina (Figure 5F; *, p = 0.03 and **, p = 0.0003, paired Student's t test). These results indicate that signal transduction from short-wavelength-sensitive cones to OFF CBCs is delayed in *Necl-1*$^{-/-}$ mouse retina.

Necl-1 is required for correct localization of AMPA receptors and for OFF cone pathways through AMPA receptors elicited by short-wavelength-light

OFF BCs express different ionotropic GluRs in mammalian retina.[31] Distinct sign-conserving types of OFF BCs anatomically and functionally express AMPA, KA, or both types of glutamate receptors on dendrites of OFF BCs in mouse retina.[32] The AMPA type-glutamate receptor subunit GluA1 (encoded by the *Gria1* gene) and the KA type-glutamate receptor subunit GluK1 (encoded by the *Grik1* gene) are expressed in OFF CBCs in mouse retina and serve important functions in signal transduction from photoreceptor cells to OFF CBCs.[32] Localization of AMPA and KA glutamate receptors was therefore examined in the outer retinas of *Necl-1*$^{-/-}$ mice. Similar immunofluorescence signal patterns for GluK1 were observed at cone pedicles labeled with PNA in both WT and *Necl-1*$^{-/-}$ mouse retinas (Figure 6A). Punctate GluA1 signals were observed mainly at the inner side of cone pedicles in WT mouse retina (Figure 6B), as previously reported.[32] In contrast to WT mouse retina, punctate GluA1 signals frequently overlapped those of PNA signals in *Necl-1*$^{-/-}$ mouse retina (Figure 6B). Furthermore, punctate GluA1 signals on the inner side of cone pedicles were significantly reduced in *Necl-1*$^{-/-}$ mouse retina compared to those in WT mouse retina (Figure 6C; **, p < 0.001, paired Student's t test).

These results indicate that Necl-1 is required for correct localization of GluA1, but not GluK1, and suggest that dislocation of GluA1 in *Necl-1*$^{-/-}$ mouse retina may be associated with a delay in signal transduction from cones to OFF CBCs (Figures 6D and 6E).

We indicated that similar physiological phenotypes in *Necl-1*$^{-/-}$ mice could be mimicked by WT mice intravitreously injected with an OFF pathway inhibitor, *cis*-2, 3-piperidinedicarboxylic acid (PDA), an *N*-methyl-D-aspartate (NMDA), AMPA, and KA receptor antagonist.[33] The peak time delay in high-frequency flicker ERGs and the amplitude decrease were also observed in PDA-injected WT mice (Figures 7A–7C; *, p = 0.03

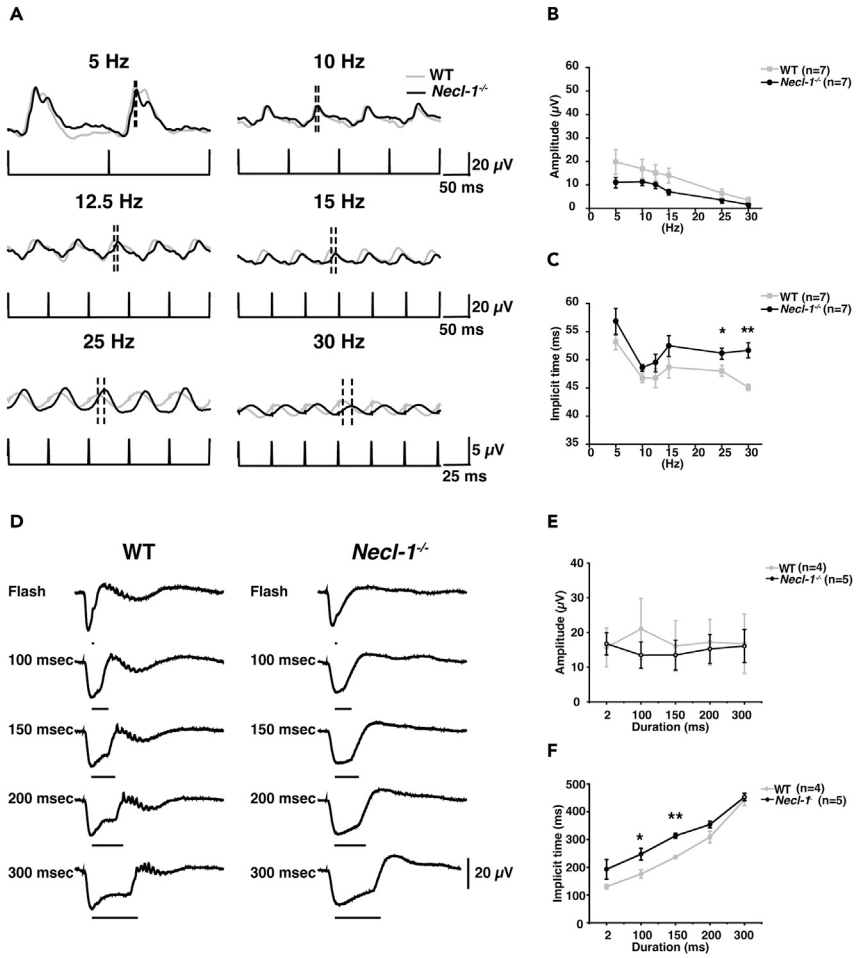

Figure 5. Role of Necl-1 in signal transduction from short-wavelength-sensitive cones to OFF CBCs

(A–C) Photopic flicker ERGs in response to UV-LED flashes. Light-adapted photopic flicker ERGs were elicited by six frequencies. (A) Representative ERGs; Black broken lines, a peak in a cycle; and lower gray line markers, UV-LED stimuli. (B) Amplitude of flicker ERGs; (C) Implicit time from trough to peak. Error bars represent ±SEM from means of $n = 7$ (WT) or $n = 7$ (*Necl-1*$^{-/-}$). *, $p = 0.03$; and **, $p = 0.002$ by paired Student's t test. (D–F) Long-duration flash ERGs after intravitreous injection of L-AP4.

(D) Representative long-duration flash ERGs; (E) Peak-to-trough amplitude of each long-duration ERGs; (F) Implicit time from trough to peak. Error bars represent ±SEM from means of $n = 4$ (WT) or $n = 5$ (*Necl-1*$^{-/-}$). *, $p = 0.03$; and **, $p = 0.0003$ by paired Student's t test. See also Figures S4–S6.

(amplitude at 15 min) and in Figure 7B, **, $p = 0.002$ and in Figure 7C, **, $p = 0.001$ (implicit time at 30 min and 45 min, respectively) by Student's t test). Then, the physiological role of Necl-1 was examined in *Necl-1*$^{-/-}$ mice by measuring UV-LED-elicited photopic flicker ERGs at 30 Hz after intravitreous injection of LY404187, an allosteric potentiator of AMPA receptors.[34] For controls, saline was injected into WT and *Necl-1*$^{-/-}$ mice and LY404187 was injected into WT mice. ERG responses were measured at 15, 30, 45, and 60 min after injection. The amplitude of ERG response in LY404187-injected *Necl-1*$^{-/-}$ mice, which was significantly larger than that of saline-injected *Necl-1*$^{-/-}$ mice 15 min post-injection, decreased to a level similar to that of saline-injected *Necl-1*$^{-/-}$ mice after 30 min (Figure 7E; *, $p = 0.01$ (LY404187 vs. saline in *Necl-1*$^{-/-}$ mice at 15 min); and **, $p = 0.003$ (*Necl-1*$^{-/-}$ vs. WT mice with saline injection at 15 min) by Wilcoxon signed-rank test.). There was no significant difference in the implicit time and amplitude of ERGs between LY404187-injected WT mice and saline-injected WT mice (Figures 7E and 7F). In addition, the implicit time of LY404187-injected *Necl-1*$^{-/-}$ mice was significantly shorter than that of saline-injected *Necl-1*$^{-/-}$ mice, 15 min after the injection, while the implicit times did not differ statistically between these two groups at 30, 45, and 60 min (Figure 7F; *, $p = 0.01$ (LY404187 in *Necl-1*$^{-/-}$ mice vs. saline in WT mice at 15 min); *, $p = 0.01$ (LY404187 vs. saline in *Necl-1*$^{-/-}$ mice at 15 min); **, $p = 0.005$ (*Necl-1*$^{-/-}$ vs. WT mice with saline injection at 15 min); *, $p = 0.03$ (*Necl-1*$^{-/-}$ vs. WT mice with saline injection at 60 min); and *, $p = 0.04$ (*Necl-1*$^{-/-}$ vs. WT mice with LY404187 injection at 60 min) by Wilcoxon signed-rank test.). These results suggest that Necl-1 was responsible for the pathway of delayed OFF responses and function of the impaired OFF pathway in *Necl-1*$^{-/-}$ mice was at least partially rescued by AMPA receptor potentiation. Collectively, these results indicate that Necl-1 mediates correct localization of GluA1 and regulates AMPA receptor-mediated signal transduction.

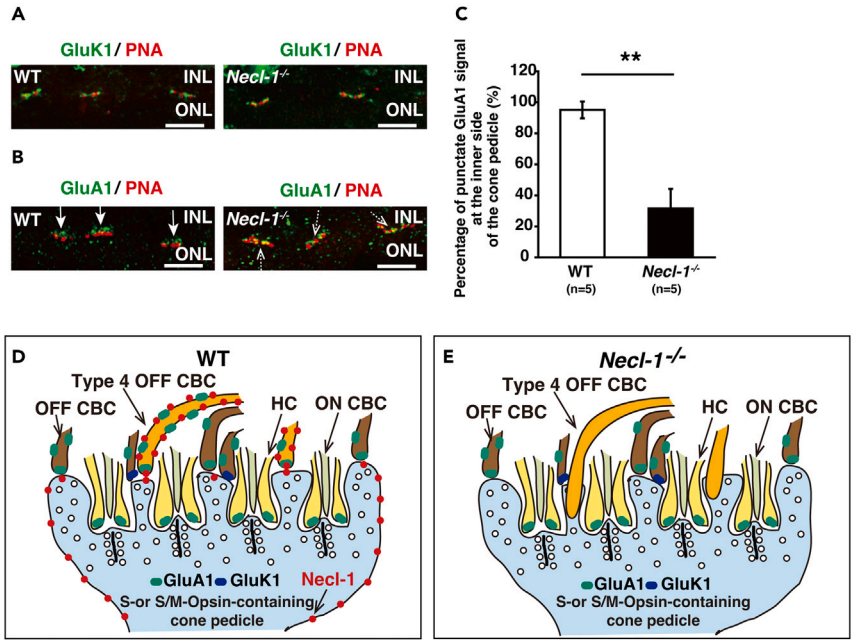

Figure 6. Role of Necl-1 in localization of AMPA receptors at synapses between cones and type 4 OFF CBCs

8-week WT and *Necl-1*$^{-/-}$ mice were used for experiments.

(A) Localization of GluK1. Retinal sections were stained with an anti-GluK1 Ab and PNA. Green, GluK1; red, PNA. Scale bars, 5 μm.

(B and C) Abnormal localization of GluA1 in *Necl-1*$^{-/-}$ mouse retina. (B) Retinal sections stained with an anti-GluA1 Ab and PNA. Green, GluA1; and red, PNA. Solid arrows and dotted arrows indicate the punctate GluA1 signal. Scale bars, 5 μm. (C) The punctate GluA1 signal at the inner side of the cone pedicle. Localization of GluA1 was analyzed. Error bars represent ±SD from means of $n = 7$ retina sections collected from individual animals ($n = 5$; WT and *Necl-1*$^{-/-}$, respectively). **, $p < 0.001$ by paired Student's t test.

(D and E) Schematic drawings of localizations of Necl-1, GluA1, and GluK1 in adult mouse retina. Transverse sectional view of the S- or S/M-opsin-containing cone pedicles in WT and *Necl-1*$^{-/-}$ mouse retinas. Red circles, Necl-1; white circles, synaptic vesicles; light yellow, HCs; light green, ON CBCs; orange, type 4 OFF CBCs; brown, OFF CBCs; green oval, GluA1; and dark blue oval, GluK1. (D) WT; (E) *Necl-1*$^{-/-}$.

Necl-1 is required for HC distribution

There are two types of HC in the retinas of most vertebrates, but in mice, there is only a single type of axon-bearing HC, which exerts lateral suppression on rods and cones.[35] We investigated the role of Necl-1 in HC morphogenesis. HCs in WT and *Necl-1*$^{-/-}$ mouse retinas were identified by immunostaining using an anti-calbindin mAb/pAb. Somata of HCs were located at the outermost part of the INL in WT mouse retina. However, calbindin-positive HC somata were dislocated to a more inner position in the ONL in *Necl-1*$^{-/-}$ mouse retina (Figure 8A). The distance between somata of calbindin-positive HCs and the position of the OPL increased significantly in *Necl-1*$^{-/-}$ mouse retina compared to that in WT mouse retina (Figure 8B; **, $p < 0.001$ by paired Student's t test.). However, the density of HCs did not differ significantly between WT and *Necl-1*$^{-/-}$ mouse retinas (Figure 8C; n.s., not significant ($p = 0.95$) by paired Student's t test.). These results indicate that somata of HCs are dislocated in *Necl-1*$^{-/-}$ mouse retina.

Positions of somata of BCs and HCs were then analyzed (Figures 8D–8G). The number of HC somata located closer to the ONL than to somata of BCs was analyzed in WT and *Necl-1*$^{-/-}$ mouse retinas. An anti-Chx10 pAb and an anti-PKCα mAb were used to identify BCs and rod BCs, respectively. The number of HC somata surrounded by BC somata was significantly larger in *Necl-1*$^{-/-}$ mouse retina than in WT mouse retina (Figures 8D–8G; in Figure 8E, *, $p = 0.02$ by paired Student's t test, in Figure 8G, *, $p = 0.04$ by paired Student's t test). These results indicate that somata of HCs are dislocated to the inner side of *Necl-1*$^{-/-}$ mouse retina.

The distribution of calbindin-positive HCs was then examined in *Necl-1*$^{-/-}$ mouse retina. Flat-mount immunostaining of mouse retina was performed to obtain z stack images containing somata and axons of HCs (Figure 8H). In the confocal image plane containing HC somata in WT mouse retina, somata and axons of HCs were present in the same volume of interest. However, in *Necl-1*$^{-/-}$ mouse retina, only somata, but not axons, were observed in the focal plane containing HC somata (Figure 8H). This dislocation of HC somata was observed in all parts of the retina. Since structures of HCs terminate in the course of development, the reaction pathway through HCs may be incomplete (Figure S7). Collectively, these results indicate that Necl-1 is required for HC distribution.

Visual function is impaired in *Necl-1*$^{-/-}$ mouse retina

We finally explored the effect of *Necl-1* deficiency on visual function at the organismal level by measuring optokinetic responses (OKRs) in the WT and *Necl-1*$^{-/-}$ mouse retinas. OKRs are reflexive eye movements observed in response to moving objects. These movements involve two

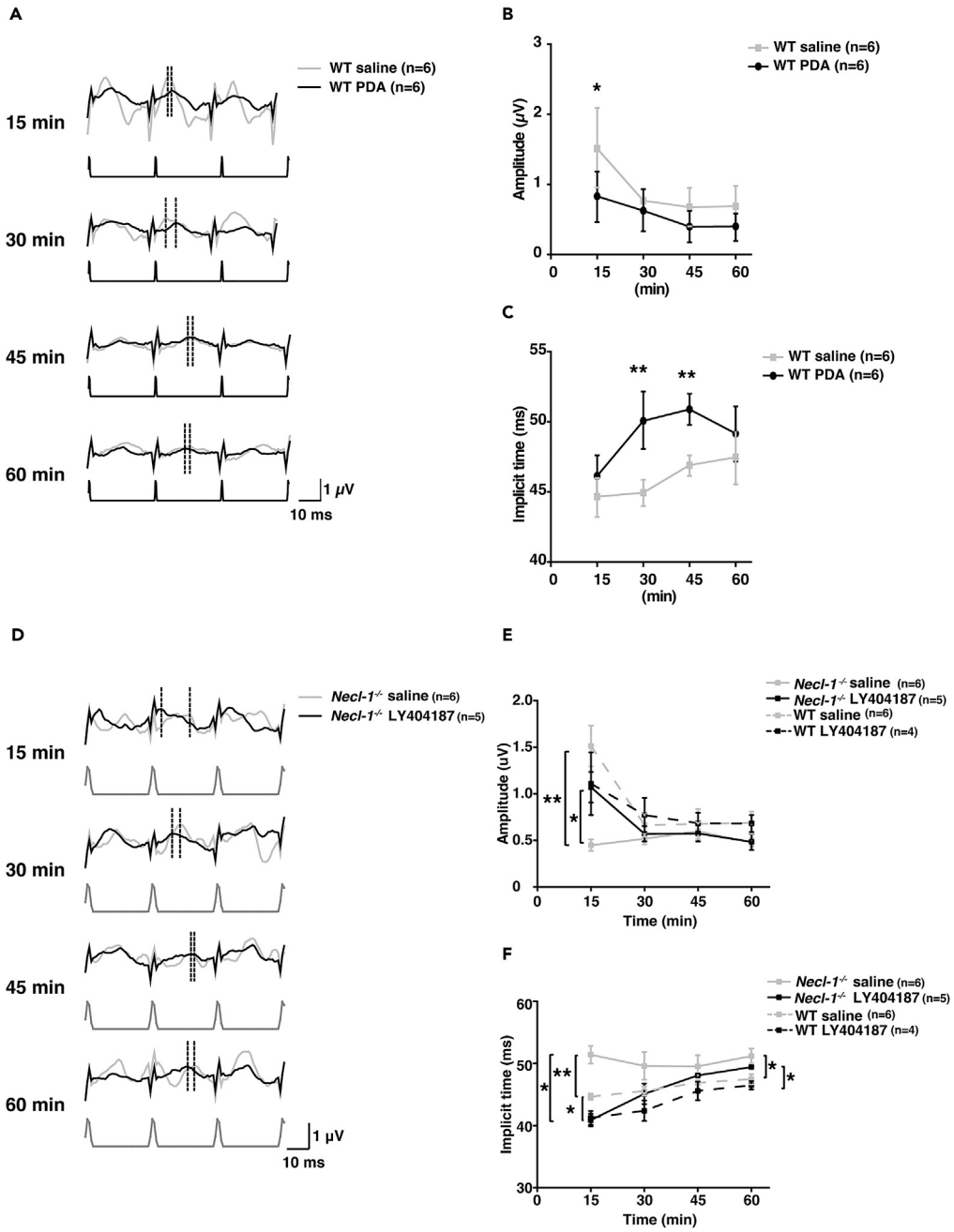

Figure 7. Role of Necl-1 in the S-opsin-mediated signaling OFF pathway via AMPA receptors

(A and B) Light-adapted photopic 30-Hz flicker ERGs in 8-week WT mice. Gray line, control saline injection; and black line, 13.15-mM PDA injection. (A) Representative light-adapted photopic 30-Hz flicker ERGs. Black broken lines, a peak in a cycle; and lower gray line markers, UV-LED stimuli. (B and C) Photopic 30-Hz flicker ERGs. Gray lines, control saline injection; and black lines, PDA injection. (B) Amplitude.

(C) Implicit time. Error bars show ±SD ($n = 6$, for the saline and PDA mice). *, $p = 0.03$ (amplitude at 15 min) and **, $p = 0.002$ and 0.001 (implicit time at 30 min and 45 min, respectively) by Student's t test.

(D–F) Time course of photopic 30-Hz flicker ERGs in response to UV-LED flashes after an intravitreous injection of the AMPA receptor potentiator, LY404187, in *Necl-1*$^{-/-}$ mice. Gray line, saline injection; and black line, LY404187 injection. (D) Representative response trace showing cycle peaks in photopic 30-Hz flicker ERGs. Both cycles were under UV-LED stimuli. (E) Amplitude of flicker ERGs. Gray line, *Necl-1*$^{-/-}$ mice with saline injection ($n = 6$); black line, *Necl-1*$^{-/-}$ mice with LY404187 injection ($n = 5$); gray broken line, WT mice with saline injection ($n = 6$), and black broken line, WT mice with LY404187 injection ($n = 4$). *,

Figure 7. *Continued*

p = 0.01 (LY404187 vs. saline in *Necl-1*$^{-/-}$ mice at 15 min); and **, $p = 0.003$ (*Necl-1*$^{-/-}$ vs. WT mice with saline injection at 15 min) by Wilcoxon signed-rank test. (F) Implicit time. *, $p = 0.01$ (LY404187 in *Necl-1*$^{-/-}$ mice vs. saline in WT mice at 15 min); *, $p = 0.01$ (LY404187 vs. saline in *Necl-1*$^{-/-}$ mice at 15 min); *, $p = 0.03$ (*Necl-1*$^{-/-}$ vs. WT mice with saline injection at 60 min); *, $p = 0.04$ (*Necl-1*$^{-/-}$ vs. WT mice with LY404187 injection at 60 min); and **, $p = 0.005$ (*Necl-1*$^{-/-}$ vs. WT mice with saline injection at 15 min) by Wilcoxon signed-rank test.

distinct phases, termed the initial and later phases.[36] The initial OKR is an open loop resulting from the function of the inner retina, comprising ON and OFF pathways, whereas the late OKR is derived from the response of the retinal circuit interacting with a feedback circuit in the brain.[37,38] Initial OKRs were measured using UV bandpass filters and under normal conditions (without filters) in WT and *Necl-1*$^{-/-}$ mouse retinas (Figures 9A–9C). OKRs were clearly observed in *Necl-1*$^{-/-}$ mouse retina and were slightly larger in *Necl-1*$^{-/-}$ mouse retina than in WT mouse retina (Figures 9D and 9E). Mean eye velocity was calculated for the initial phase (open loop; 100–200 ms) and revealed that the amplitude of the initial OKR obtained with or without UV band-pass filters was larger in *Necl-1*$^{-/-}$ mice than in WT mice (Figures 9F and 9G; *, $p = 0.015$; and **, $p = 0.0074$ by paired Student's t test.). These results indicate that Necl-1 is required for normal visual function in mouse retina.

DISCUSSION

In this study, we first showed that Necl-1 is localized at almost all S-opsin-positive cones, half of M-opsin-positive cones and dendrites of type 4 OFF CBCs near cone pedicles. In mouse retina, many cone photoreceptors co-express S-opsin and M-opsin, S/M cones.[39] In addition, because it was previously shown that 4 subtypes of OFF CBCs, including type 4, connect to S-cones and M-cones,[40,41] Necl-1 is likely to be important role in morphological connections between type 4 OFF CBCs and cones in which S-opsin is expressed, S- and S/M-opsin-containing cones.

Synaptic organization of the OPL is elaborate and intricate. We next showed that Necl-1 is essential for the S-opsin-mediated signaling OFF pathway through AMPA receptors in the OPL. In the mouse retina, type 2, 3a, 3b, and 4 OFF CBCs and type 6, 7, and 9 ON CBCs are connected with S cones.[40,41] A single-cell RNA profiling analysis recently showed that *Necl-1/CADM3* is expressed throughout the retina, especially in ACs, cone photoreceptors, OFF CBCs, mainly type 4 CBCs, and type 8/9 ON CBCs.[22] In the present study, we showed that Necl-1 is expressed in OFF CBCs; predominantly type 4, and some type 3a and 3b. In addition, whole-mount immunostaining analysis indicated that Necl-1 is abundantly localized in bipolar cells in ventral retina. These results may indicate that Necl-1 is expressed in bipolar cells connected with S- and S/M-opsin-containing cones. Different types of OFF CBCs express different combinations of ionotropic glutamate receptor types on their dendrites. AMPA-type receptors (GluA1) are expressed at type 1, 3b, and 4 OFF CBCs, whereas type 2, 3a, 3b, and 4 OFF CBCs express kainite receptors (GluK1).[42] We found that genetic ablation of *Necl-1* caused dislocation of type 4 OFF CBC dendrites, not other types of OFF CBCs, and resulted in dislocation of the AMPA receptor subunit, GluA1.

Nectin superfamily members homophilically or heterophilically *trans*-interact. Indeed, Necl-1 *trans*-interacts not only with Necl-1 but also with Necl-2, Necl-3, Necl-4, nectin-1, and nectin-3.[21] We recently identified a novel adhesion apparatus, named the "nectin-1 spot", which tethers lateral dendrites of mitral cells and regulates their branching in developing mouse olfactory bulb.[43–45] The nectin-1 spot shows that Nectin-1 molecules homophilically *trans*-interact, and are not associated with afadin, an intracellular nectin-binding protein, nor with cadherins or their intracellular binding proteins, nor with the electron-dense cytoskeletal undercoat.[44] We propose that the Necl-1-mediated cell adhesion apparatus in the OPL is similar to that of the nectin-1 spot; thus, we refer to it in the following discussion as the "Necl-1 spot." Necl-1 proteins may homophilically *trans*-interact at contact sites between dendrites of type 4 OFF CBCs and basal contacts of cone pedicles, because excessive type 4 CBC dendrites extend into the outer retinal side and the GluA1 signal at the inner side of cone pedicles was significantly reduced in *Necl-1*$^{-/-}$ mouse retina. A recent study showed that Cadm3-mediated homophilic interaction provides an intercellular mechanism underlying coordinated cell proliferation and ensures cell number homeostasis of developing neuroepithelia in zebrafish retina.[46] In mouse retina, Cadm-3-mediated homophilic interaction may also be important in cell proliferation at the early proliferative stage. This evidence supports the symmetric distribution of Necl-1 observed in Necl-1 spots. However, it needs further study to determine whether Necl-1 proteins homophilically or heterophilically *trans*-interact at the plasma membrane of cones and dendrites of type 4 OFF CBCs. While the *trans*-interacting partner of Necl-1 remains unidentified, it may be one or more other members of the nectin superfamily.

Next, we examined the functional role of Necl-1 using electroretinograms (ERGs). *Necl-1* deficiency did not cause any significant abnormality in standard ERGs under either scotopic or photopic conditions and flicker ERGs with white LED stimulation which stimulates mainly M-opsin. However, UV-LED-elicited flicker ERGs, which isolate the S-opsin-mediated OFF pathway, did show a significant peak delay at frequencies of 25 and 30 Hz in *Necl-1*$^{-/-}$ mouse retina, with the delay at 30 Hz rescued by intravitreous injection of the allosteric AMPA receptor potentiator, LY404187 into eyes of *Necl-1*$^{-/-}$ mice. These results indicate that Necl-1 is essential for OFF cone pathways through AMPA receptors elicited by short-wavelength light. M-opsin can to some extent respond to UV light because M-opsin has spectrum sensitivity in the UV spectrum (Figure S6).[47] However, we previously showed that M-opsin-induced photopic response obtained at a luminance below 2.7 log $\mu W \cdot ms/cm^2$ is very small.[29] So, we selected a UV luminance of 202.8 $\mu W\ ms/cm^2$ (2.3 log $\mu W \cdot ms/cm^2$) in this report. This is the reason that UV-LED-elicited-flicker ERGs analysis demonstrated an impaired S-opsin-mediated OFF pathway in *Necl-1*$^{-/-}$ mice.

Necl-1 contains domain structures like those of other members of the nectin/Necl superfamily: three immunoglobulin-like domains in an extracellular region, a single transmembrane region, and a cytoplasmic region.[48] Notably, Necl-1 contains a FERM domain in its cytoplasmic region.[48] The FERM domain binds to Band 4.1 (Epb4.1) proteins, including Band 4.1N. Accordingly, Necl-1 may serve important functions in synaptic architecture and function by associating with the F-actin cytoskeleton through protein 4.1N and it may be involved in morphological

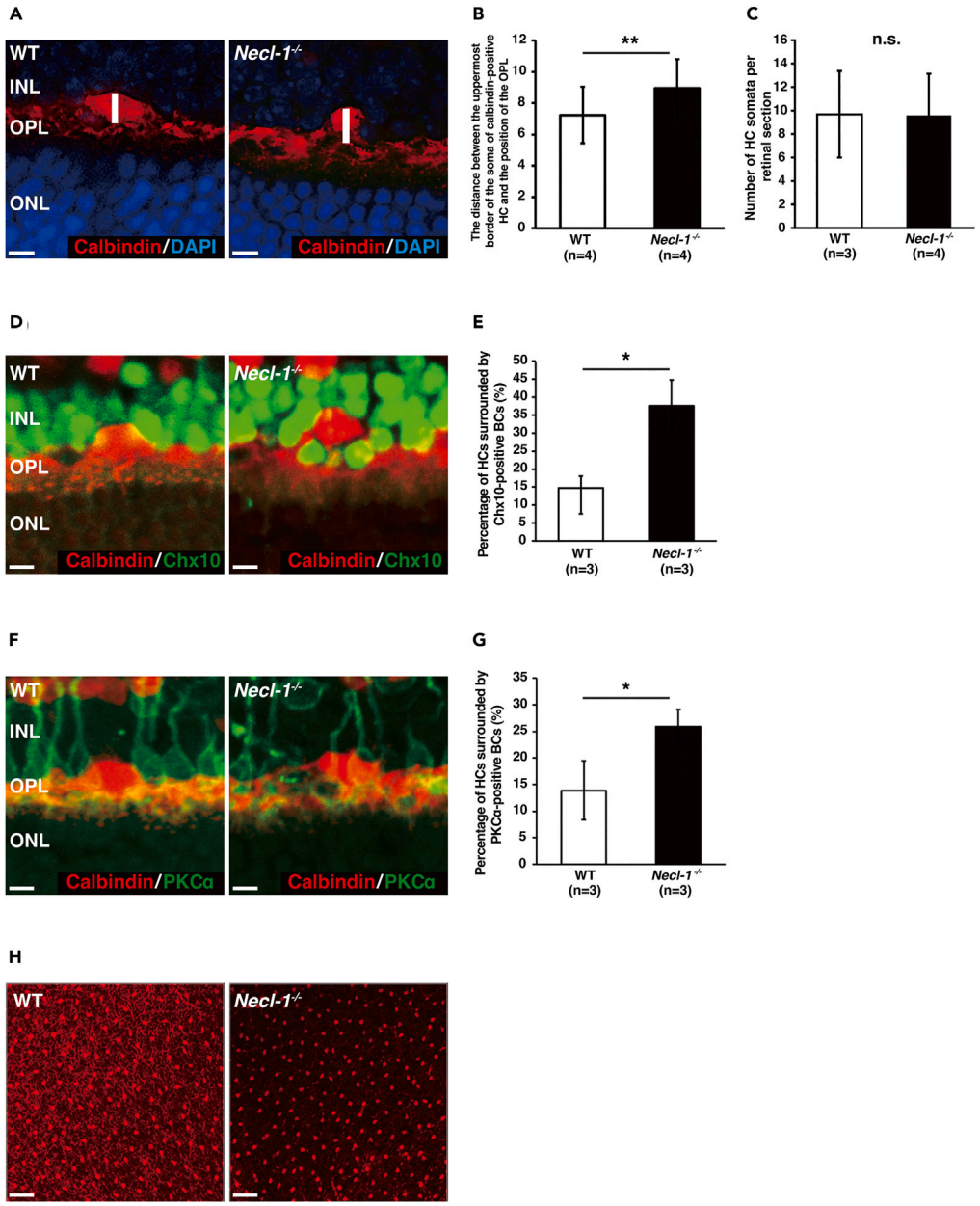

Figure 8. Abnormal distribution of HCs caused by *Necl-1* ablation

Immunohistochemical analysis of 8-week WT and *Necl-1*$^{-/-}$ mouse retinas.

(A–C) Abnormal distribution of calbindin-positive HCs in the *Necl-1*$^{-/-}$ mouse retina. (A) Calbindin-positive HCs in the OPL. The anti-calbindin mAb/pAb was used. Red, calbindin; and blue, DAPI. The white line indicates the distance between the uppermost border of the soma of a calbindin-positive HC and the position of the OPL. (B) The average distance between the uppermost border of somas of calbindin-positive HCs and the position of the OPL in WT and *Necl-1*$^{-/-}$ mouse retinas. A total of 36 horizontal cells were measured in WT or *Necl-1*$^{-/-}$, respectively. **, $p < 0.001$ by paired Student's t test. Error bars represent ±SD from means of $n = 4$ (WT and *Necl-1*$^{-/-}$, respectively). (C) Numbers of HC somata per retinal section. Error bars represent ±SD from means of $n = 6$ to 11 retina sections collected from individual animals ($n = 3$ and 4; WT and *Necl-1*$^{-/-}$, respectively). n.s., not significant ($p = 0.95$) by paired Student's t test.

(D–G) Increase in numbers of HC somata surrounded by BC somata in *Necl-1*$^{-/-}$ mouse retina. Numbers of HC somata surrounded by Chx10-positive or PKCα-positive BC somata were counted. (D and E) HCs surrounded by somata of Chx10-positive BCs. (D) Calbindin-positive HCs and Chx10-positive BCs in the INL and OPL. The anti-calbindin mAb and the anti-Chx10 pAb were used. Green, Chx10; and red, calbindin. (E) Percentage of HC somata surrounded by Chx10-positive BC somata in the WT and *Necl-1*$^{-/-}$ mouse retinas. Error bars represent ±SD from means of $n = 36$ horizontal cells collected from individual animals $n = 3$ (WT and *Necl-1*$^{-/-}$, respectively). *, $p = 0.02$ by paired Student's t test. (F and G) HCs surrounded by somata of PKCα-positive BCs. (F) Calbindin-positive HCs and PKCα-positive BCs in the INL and OPL. The anti-calbindin pAb and the anti-PKCα mAb were used. Green, PKCα; and red,

Figure 8. *Continued*

calbindin. (G) Percentage of HC somata surrounded by PKCα-positive BC somata in WT and *Necl-1*$^{-/-}$ mouse retinas. Error bars represent ±SD from means of n = 36 horizontal cells collected from individual animals n = 3 (WT and *Necl-1*$^{-/-}$, respectively). *, p = 0.04 by paired Student's t test.

(H) Whole-mount immunostaining of WT and *Necl-1*$^{-/-}$ mouse retinas. The anti-calbindin mAb was used. Each immunofluorescence signal was collected horizontally from the plane containing HC somata to the plane containing the OPL. Scale bars, 5 μm in A, D, and F; and 50 μm in H. See also Figure S7.

development, stability, and dynamic plasticity of the nervous system.[49] Band 4.1N also binds to AMPA receptors (GluA1) and to the actin cytoskeleton,[50] whereas Band 4.1G contributes to rod synaptic location.[51] These findings suggest that Necl-1 is important for correct localization of AMPA receptors in the OFF pathway during development of cones by binding to AMPA receptors via Band 4.1N. However, it remains uncertain whether the allosteric AMPA receptor potentiator, LY404187, affects only AMPA receptors on CBCs, because they are expressed in other cells throughout the retina.

To evaluate how *Necl-1* ablation affects mouse visual function, we designed and examined initial OKRs using UV band-path filters, through which only short-wavelength light (200–400 nm) can pass (central wavelength, 330 nm). *Necl-1*$^{-/-}$ mouse retina showed a larger gain in the initial OKR compared to WT mouse retina, either with or without UV band-pass filters. In vertebrate retina, HCs and ACs, two types of retinal interneurons, modulate signaling from photoreceptors to bipolar cells in the OPL and from bipolar cells to RGCs in the IPL, respectively. ACs have critical roles in visual processing, but the HC contribution to visual information processing is still limited. HCs mediate the cone-driven lateral interaction pathway in the photopic condition,[52] and regulate antagonistic center-surround receptive field organization in the outer retina.[10] Recently, Chaya et al. indicated that HC loss reduces formation of the antagonistic receptive field surrounding RGCs in HC-depleted mice, which is not compensated by inhibitory activities of ACs in the IPL.[12] HC loss impairs global light adaptation at the retinal output level and shows a lower shift of optimal spatial frequency of visual motion. Chaya et al. also found that HC loss achieved a larger gain in the initial OKR,[12] similar to our results. *Necl-1*$^{-/-}$ mouse retina in the present study had an abnormal distribution of HCs and a larger amplitude of the initial OKR obtained with or without UV band-pass filters. HC vertical migration is regulated by genetic pathways in developing retina.[53] Intracellular spacing is controlled by homotypic interactions occurring at the earliest stages. Developing HCs extend their dendritic fields to establish constant coverage of the retina. Connectivity between horizontal cells and cone pedicles changes during development, acquiring or eliminating contacts as a function of relative distance.[54] The LIM homeodomain transcription factor, *Lim1*, is critical for HC positioning. Absence of *Lim1* function causes an increase in dendrite receptive fields, branching, and terminal clusters due to reduced regularity and homology in nuclear arrangement. In other words, they are regulated by connections between homophilic and afferent horizontal cells.[55] Since Necl-1 expression is not detected in HCs, the abnormal distribution of HCs may be a secondary effect resulting from Necl-1 loss in ACs and OFF BCs. While we have not clarified whether *Necl-1*$^{-/-}$ mice exhibit abnormalities of HC dendritic fields or terminal clusters, we speculate that HC migration at developmental stages may be disturbed in KO mice, leading to immature HC function, as in HC-depleted mice. This results in a larger response in reflexive eye movements in the initial phase after visually sensing a moving visual pattern. Thus, our results suggest that Necl-1 is involved in visual function. Further studies are needed to develop a more detailed molecular mechanism about visual information processing mediated by HCs in *Necl-1*$^{-/-}$ mouse retina.

Limitations of the study

The single-cell RNA profiling analysis in the current study showed that Necl-1 is expressed in some ACs of the inner retina.[22] While it can be speculated that AMPA receptors are dislocated in the inner retina, including GCLs, this issue is beyond the scope of the present study.

It was previously shown that Necl-1 is localized in the IPL in the retina in zebrafish and mice,[2,24] but Necl-1 localization in mouse outer retina has not been reported yet. Thus, in the present study, we investigated localization and function of Necl-1 in mouse outer retina. Our results showed that Necl-1 affects synaptogenesis between cones and type 4 CBCs and is involved in localization of AMPA receptors. When Necl-1 was deleted, the weak adhesion between CBC synaptic plexuses remained, but AMPA receptors were dislocated far from their original positions, suggesting that glutamate released from ribbon synapses diffuses to glutamate receptors, causing a delay in the implicit time in flicker ERGs, although glutamate finally reaches glutamate receptors and does not change the magnitude of the ERG response. Analysis with a wide-area electron microscope could clarify the correlation between function and structure by analogy at this point. It is not yet clear whether simultaneous abnormal HC distribution is associated with impairment of visual function. Necl-1 is also expressed in ACs, so the abnormality of visual function in OKRs in *Necl-1*$^{-/-}$ mice may be caused by visual processing in the IPL.

Although differences likely exist between Necl-1 function in mice and humans, the present results suggest that *NECL-1* dysfunction in the retinal OPL may cause visual abnormalities. However, we cannot exclude the possibility that these visual abnormalities may be caused by *Necl-1* deficiency at another site of retina and brain, and the only proposed retinal mechanisms cannot simply explain color vision properties. That is because the mechanism of color discrimination in mice involves opponent processing of cone photoreceptor signals and also the lateral geniculate nucleus (LGN).[56] Further studies using tissue-specific *Necl-1* conditional knockout mice are required to clarify this issue.

STAR★METHODS

Detailed methods are provided in the online version of this paper and include the following:

- KEY RESOURCES TABLE
- RESOURCE AVAILABILITY
  - Lead contact

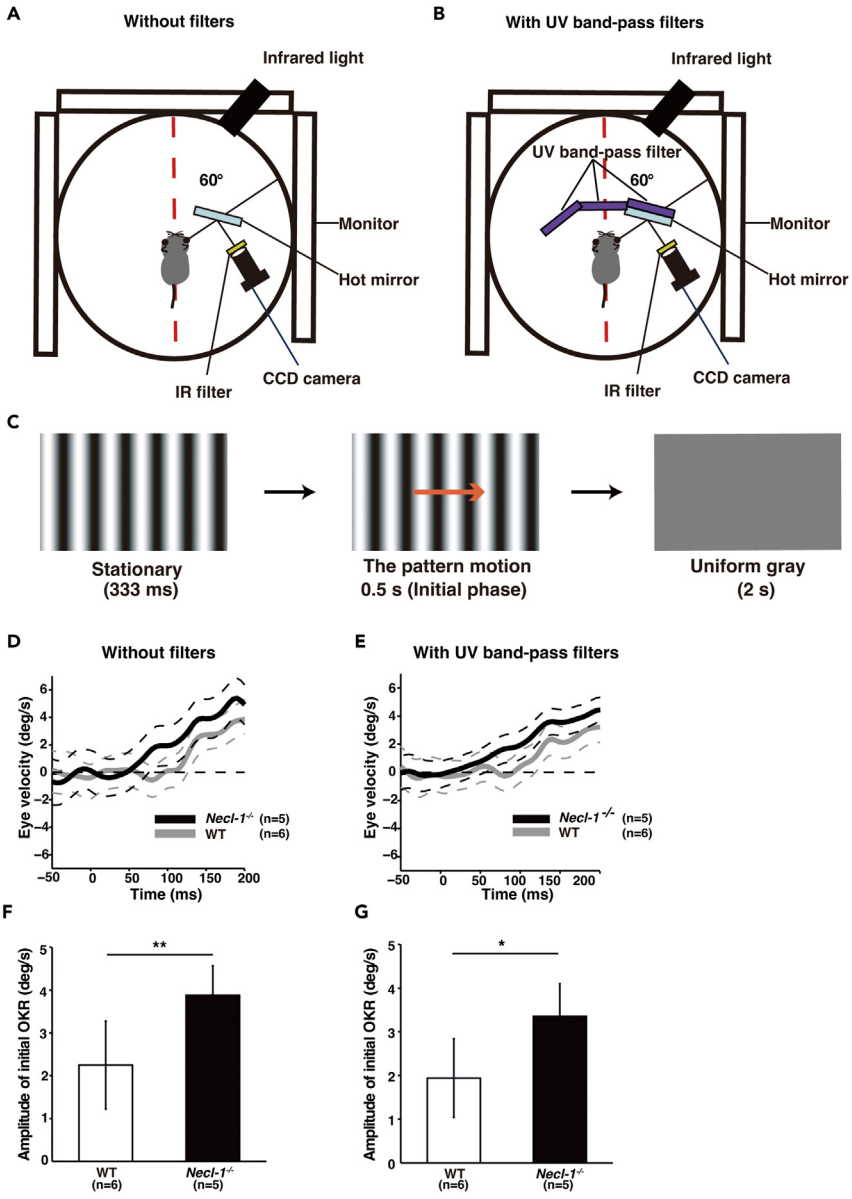

Figure 9. Optokinetic responses to motion of sinusoidal gratings

8-week WT and *Necl-1*$^{-/-}$ mice were used for these experiments.

(A and B) Diagrams showing experimental equipment used to record mouse eye movements. Infrared images of the right eye were collected using a charge-coupled device (CCD) camera. To expose the entire visual field of mice to short-wavelength light (blue color) stimuli, three UV band-pass filters were positioned in front of mice. (A) Experimental setup without filters. (B) Setup with UV band-pass filters.

(C) Experimental scheme. First, a stationary visual pattern was presented, followed by presentation of a counterclockwise (temporal-nasal motion for the right eye) or clockwise (nasal-temporal motion for the right eye) moving visual pattern at a constant speed. After a defined period, the pattern was removed.

(D and E) Eye velocity profiles. Gray solid line, WT mice ($n = 6$); and black solid line, *Necl-1*$^{-/-}$ mice ($n = 5$). (D) Without filters; (E) With UV band-pass filters. Broken lines indicate the standard error of the mean. "Time zero" denotes the onset time of visual motion.

(F and G) Mean eye velocity during the open-loop phase of visual stimuli under the normal or UV condition. (F) During presentation of visual stimuli without filters; or (G) with UV band-pass filters. Error bars represent ±SD from means of $n = 6$ (WT) or $n = 5$ (*Necl-1*$^{-/-}$). *, $p = 0.015$; and **, $p = 0.0074$ by paired Student's t test.

SUPPLEMENTAL INFORMATION

Supplemental information can be found online at https://doi.org/10.1016/j.isci.2024.109577.

ACKNOWLEDGMENTS

This study was supported by JSPS KAKENHI (Japan Society for the Promotion of Science Grants-in-Aid for Scientific Research) grant numbers JP25253093 (K.N.), JP26462686, JP18K09406 (K.Mat.), JP21K06177 (K.Man.), JP21H02657 (T.F.), and JP26251013 (Y.T.); JSPS KAKENHI Grants-in-Aid for Scientific Research C (No. JP18K09406) (K.M.), and Grants-in-Aid for Early-Career Scientists JP20K18379 (R.K.); MEXT KAKENHI (Ministry of Education, Culture, Sports, Science, and Technology Grants-in-Aid for Scientific Research) grant numbers JP26114007 (Y.T.) and JP16H06463 (K.Man.); and AMED-CREST (Japan Agency for Medical Research and Development Core Research for Evolutional Science and Technology) under Grant Number 21-23gm1210004 (K.N.). The authors thank Jun Miyoshi (Osaka International Cancer Institute) for generation of the *Necl-1* knockout mouse line. We gratefully acknowledge Hideaki Yamamoto and Hajime Shiotani (Kobe University) and Rikako Sanuki (Kyoto Institute of Technology) for technical assistance and scientific discussions. Hidetaka Kudo and Masao Yoshikawa (Mayo Co., Ltd.), Tomomitsu Miyoshi (Osaka University), and Hajime Sawai (Osaka Prefectural University) provided invaluable technical support with ERG equipment in Center for Medical Research and Education, Graduate School of Medicine, Osaka University, and Takashi Fujikado (Osaka University) kindly provided technical and critical discussions. We thank Steven D. Aird (www.sda-technical-editor.org) for editing the later drafts of this manuscript, and also Jeremy Allen, PhD, and Doran Amos, PhD, from Edanz Group (www.edanzediting.com/ac) for editing the first draft of this manuscript.

We acknowledge the acquisition of the single-cell RNA-seq data in the Study: Retinal Bipolar Neuron Drop-seq from Single-cell portal website provided by the Broad Institute (Cambridge, MA, USA).[22]

AUTHOR CONTRIBUTIONS

R.K., K.Mat., K.Man., T.M., K.Miz., A.M., T.F., K.N., and Y.T. designed the project. R.K. performed the *in vitro* and immunohistochemistry experiments and analyzed the data. R.K., K.Mat., and K.K. performed ERG recordings and analyzed the data. Y.M. and R.S. developed 3D image analysis software and analyzed the whole-mount staining to detect the dorsoventral distribution of Necl-1-positive cells. Y.S. and T.F. performed OKR recordings and analyzed data. A.O. and Y.M. performed single-cell RNA-seq data subanalysis. R.K., K.Mat., K.Man., A.M., T.F., and Y.T. wrote the paper. K.Mat. and Y.T. supervised the project. All authors have reviewed the manuscript.

DECLARATION OF INTERESTS

The authors declare no competing interests.

Received: September 19, 2022
Revised: December 22, 2023
Accepted: March 25, 2024
Published: March 26, 2024

REFERENCES

1. Röhlich, P., van Veen, T., and Szél, A. (1994). Two different visual pigments inone retinal cone cell. Neuron *13*, 1159–1166. https://doi.org/10.1016/0896-6273(94)90053-1.
2. Hunt, D.M., and Peichl, L. (2014). S cones: Evolution, retinal distribution,development and spectral sensitivity. Vis. Neurosci. *31*, 115–138. https://doi.org/10.1017/S0952523813000242.
3. Schiller, P.H. (1992). The ON and OFF channels of the visual system. Trends Neurosci. *15*, 86–92. https://doi.org/10.1016/0166-2236(92)90017-3.
4. Schiller, P.H. (2010). Parallel information processing channels created in the retina. SA *107*, 17087–17094. https://doi.org/10.1073/pnas.1011782107.
5. Werblin, F.S., and Dowling, J.E. (1969). Organization of the retina of the mudpuppy, Necturus maculosus. II.

Intracellular recording. J. Neurophysiol. *32*, 339–355. https://doi.org/10.1152/jn.1969.32.3.339.

6. Nakanishi, S., Nakajima, Y., Masu, M., Ueda, Y., Nakahara, K., Watanabe, D., Yamaguchi, S., Kawabata, S., and Okada, M. (1998). Glutamate receptors: brain function and signal transduction. Brain Res. Brain Res. Rev. *26*, 230–235. https://doi.org/10.1016/s0165-0173(97)00033-7.
7. Morigiwa, K., and Vardi, N. (1999). Differential expression of ionotropic glutamate receptor subunits in the outer retina. J. Comp. Neurol. *405*, 173–184. https://doi.org/10.1002/(sici)1096-9861(19990308)405:2<173::aid-cne3>3.0.co;2-l.
8. Koike, C., Obara, T., Uriu, Y., Numata, T., Sanuki, R., Miyata, K., Koyasu, T., Ueno, S., Funabiki, K., Tani, A., et al. (2010). TRPM1 is a component of the retinal ON bipolar cell transduction channel in the mGluR6 cascade. SA *107*, 332–337. https://doi.org/10.1073/pnas.0912730107.
9. Shelley, J., Dedek, K., Schubert, T., Feigenspan, A., Schultz, K., Hombach, S., Willecke, K., and Weiler, R. (2006). Horizontal cell receptive fields are reduced in connexin57-deficient mice. Eur. J. Neurosci. *23*, 3176–3186. https://doi.org/10.1111/j.1460-9568.2006.04848.x.
10. Thoreson, W.B., and Mangel, S.C. (2012). Lateral interactions in the outer retina. Prog. Retin. Eye Res. *31*, 407–441. https://doi.org/10.1016/j.preteyeres.2012.04.003.
11. Liu, X., Hirano, A.A., Sun, X., Brecha, N.C., and Barnes, S. (2013). Calcium channels in rat horizontal cells regulate feedback inhibition of photoreceptors through an unconventional GABA- and pH-sensitive mechanism. J. Physiol. *591*, 3309–3324. https://doi.org/10.1113/jphysiol.2012.248179.
12. Chaya, T., Matsumoto, A., Sugita, Y., Watanabe, S., Kuwahara, R., Tachibana, M., and Furukawa, T. (2017). Versatile functional roles of horizontal cells in the retinal circuit. Sci. Rep. *7*, 5540. https://doi.org/10.1038/s41598-017-05543-2.
13. Chapot, C.A., Euler, T., and Schubert, T. (2017). How do horizontal cells 'talk' to cone photoreceptors? Different levels of complexity at the cone-horizontal cell synapse. J. Physiol. *595*, 5495–5506. https://doi.org/10.1113/JP274177.
14. Baier, H. (2013). Synaptic laminae in the visual system: molecular mechanisms forming layers of perception. Annu. Rev. Cell Dev. Biol. *29*, 385–416. https://doi.org/10.1146/annurev-cellbio-101011-155748.
15. Hattori, D., Millard, S.S., Wojtowicz, W.M., and Zipursky, S.L. (2008). Dscam-mediated cell recognition regulates neural circuit formation. Annu. Rev. Cell Dev. Biol. *24*, 597–620. https://doi.org/10.1146/annurev.cellbio.24.110707.175250.
16. Hoon, M., Bauer, G., Fritschy, J.M., Moser, T., Falkenburger, B.H., and Varoqueaux, F. (2009). Neuroligin 2 controls the maturation of GABAergic synapses and information processing in the retina. J. Neurosci. *29*, 8039–8050. https://doi.org/10.1523/JNEUROSCI.0534-09.2009.
17. Iwai, Y., Hirota, Y., Ozaki, K., Okano, H., Takeichi, M., and Uemura, T. (2002). DN-cadherin is required for spatial arrangement of nerve terminals and ultrastructural organization of synapses. Mol. Cell. Neurosci. *19*, 375–388. https://doi.org/10.1006/mcne.2001.1081.
18. Yamagata, M., and Sanes, J.R. (2008). Dscam and Sidekick proteins direct lamina-specific synaptic connections in vertebrate retina. Nature *451*, 465–469. https://doi.org/10.1038/nature06469.
19. Sanes, J.R., and Zipursky, S.L. (2020). Synaptic specificity, recognition molecules, and assembly of neural circuits. Cell *181*, 536–556. https://doi.org/10.1016/j.cell.2020.04.008.
20. Mandai, K., Rikitake, Y., Mori, M., and Takai, Y. (2015). Nectins and nectin-like molecules in development and disease. Curr. Top. Dev. Biol. *112*, 197–231. https://doi.org/10.1016/bs.ctdb.2014.11.019.
21. Takai, Y., Miyoshi, J., Ikeda, W., and Ogita, H. (2008). Nectins and nectin-like molecules: roles in contact inhibition of cell movement and proliferation. Nat. Rev. Mol. Cell Biol. *9*, 603–615. https://doi.org/10.1038/nrm2457.
22. Shekhar, K., Lapan, S.W., Whitney, I.E., Tran, N.M., Macosko, E.Z., Kowalczyk, M., Adiconis, X., Levin, J.Z., Nemesh, J., Goldman, M., et al. (2016). Comprehensive classification of retinal bipolar neurons by single-cell transcriptomics. Cell *166*, 1308–1323.e30. https://doi.org/10.1016/j.cell.2016.07.054.
23. Ribic, A., Liu, X., Crair, M.C., and Biederer, T. (2014). Structural organization and function of mouse photoreceptor ribbon synapses involve the immunoglobulin protein synaptic cell adhesion molecule 1. J. Comp. Neurol. *522*, 900–920. https://doi.org/10.1002/cne.23452.
24. Park, J., Liu, B., Chen, T., Li, H., Hu, X., Gao, J., Zhu, Y., Zhu, Q., Qiang, B., Yuan, J., et al. (2008). Disruption of Nectin-like 1 cell adhesion molecule leads to delayed axonal myelination in the CNS. J. Neurosci. *28*, 12815–12819. https://doi.org/10.1523/JNEUROSCI.2665-08.2008.
25. Hunter, P.R., Nikolaou, N., Odermatt, B., Williams, P.R., Drescher, U., and Meyer, M.P. (2011). Localization of Cadm2a and Cadm3 proteins during development of the zebrafish nervous system. J. Comp. Neurol. *519*, 2252–2270. https://doi.org/10.1002/cne.22627.
26. Kakunaga, S., Ikeda, W., Itoh, S., Deguchi-Tawarada, M., Ohtsuka, T., Mizoguchi, A., and Takai, Y. (2005). Nectin-like molecule-1/TSLL1/SynCAM3: a neural tissue-specific immunoglobulin-like cell-cell adhesion molecule localizing at non-junctional contact sites of presynaptic nerve terminals, axons and glia cell processes. J. Cell Sci. *118*, 1267–1277. https://doi.org/10.1242/jcs.01656.
27. Rich, K.A., Zhan, Y., and Blanks, J.C. (1997). Migration and synaptogenesis of cone photoreceptors in the developing mouse retina. J. Comp. Neurol. *388*, 47–63.
28. Tanimoto, N., Sothilingam, V., Kondo, M., Biel, M., Humphries, P., and Seeliger, M.W. (2015). Electroretinographic assessment of rod- and cone-mediated bipolar cell pathways using flicker stimuli in mice. Sci. Rep. *5*, 10731. https://doi.org/10.1038/srep10731.
29. Kawashima, R., Matsushita, K., Kuniyoshi, K., and Nishida, K. (2019). Contribution of bipolar cells of cone ON and OFF pathways to electroretinograms elicited by ultraviolet and middle wavelength stimuli. Curr. Eye Res. *44*, 413–422. https://doi.org/10.1080/02713683.2018.1549262.
30. Ueno, A., Omori, Y., Sugita, Y., Watanabe, S., Chaya, T., Kozuka, T., Kon, T., Yoshida, S., Matsushita, K., Kuwahara, R., et al. (2018). Lrit1, a retinal transmembrane protein, regulates selective synapse formation in cone photoreceptor cells and visual acuity. Cell Rep. *22*, 3548–3561. https://doi.org/10.1016/j.celrep.2018.03.007.
31. Brandstätter, J.H., and Hack, I. (2001). Localization of glutamate receptors at a complex synapse. Cell Tissue Res. *303*, 1–14. https://doi.org/10.1007/s004410000304.
32. Puller, C., Ivanova, E., Euler, T., Haverkamp, S., and Schubert, T. (2013). OFF bipolar cells express distinct types of dendritic glutamate receptors in the mouse retina. Neuroscience *243*, 136–148. https://doi.org/10.1016/j.neuroscience.2013.03.054.
33. Slaughter, M.M., and Miller, R.F. (1983). An excitatory amino acid antagonist blocks cone input to sign-conserving second-order retinal neurons. Science *219*, 1230–1232. https://doi.org/10.1126/science.6131536.
34. Quirk, J.C., and Nisenbaum, E.S. (2002). LY404187: a novel positive allosteric modulator of AMPA receptors. CNS Drug Rev. *8*, 255–282. https://doi.org/10.1111/j.1527-3458.2002.tb00228.x.
35. Peichl, L., and González-Soriano, J. (1994). Morphological types of horizontal cell in rodent retinae: a comparison of rat, mouse, gerbil, and guinea pig. Vis. Neurosci. *11*, 501–517. https://doi.org/10.1017/s095252380000242x.
36. Stahl, J.S. (2004). Using eye movements to assess brain function in mice. Vision Res. *44*, 3401–3410. https://doi.org/10.1016/j.visres.2004.09.011.
37. Sugita, Y., Miura, K., Araki, F., Furukawa, T., and Kawano, K. (2013). Contributions of retinal direction-selective ganglion cells to optokinetic responses in mice. Eur. J. Neurosci. *38*, 2823–2831. https://doi.org/10.1111/ejn.12284.
38. Tabata, H., Shimizu, N., Wada, Y., Miura, K., and Kawano, K. (2010). Initiation of the optokinetic response (OKR) in mice. J. Vis. *10*, 1–17. https://doi.org/10.1167/10.1.13.
39. Applebury, M.L., Antoch, M.P., Baxter, L.C., Chun, L.L., Falk, J.D., Farhangfar, F., Kage, K., Krzystolik, M.G., Lyass, L.A., and Robbins, J.T. (2000). The murine cone photoreceptor: a single cone type expresses both S and M opsins with retinal spatial patterning. Neuron *27*, 513–523. https://doi.org/10.1016/s0896-6273(00)00062-3.
40. Behrens, C., Schubert, T., Haverkamp, S., Euler, T., and Berens, P. (2016). Connectivity map of bipolar cells and photoreceptors in the mouse retina. Elife *5*, e20041. https://doi.org/10.7554/eLife.20041.
41. Breuninger, T., Puller, C., Haverkamp, S., and Euler, T. (2011). Chromatic bipolar cell pathways in the mouse retina. J. Neurosci. *31*, 6504–6517. https://doi.org/10.1523/JNEUROSCI.0616-11.2011.
42. Euler, T., Haverkamp, S., Schubert, T., and Baden, T. (2014). Retinal bipolar cells: elementary building blocks of vision. Nat. Rev. Neurosci. *15*, 507–519. https://doi.org/10.1038/nrn3783.
43. Fujiwara, T., Inoue, T., Maruo, T., Rikitake, Y., Ieki, N., Mandai, K., Kimura, K., Kayahara, T., Wang, S., Itoh, Y., et al. (2015). Nectin-1 spots regulate the branching of olfactory mitral cell dendrites. Mol. Cell. Neurosci. *68*, 143–150. https://doi.org/10.1016/j.mcn.2015.07.003.
44. Inoue, T., Fujiwara, T., Rikitake, Y., Maruo, T., Mandai, K., Kimura, K., Kayahara, T., Wang, S., Itoh, Y., Sai, K., et al. (2015). Nectin-1 spots as a novel adhesion apparatus that tethers mitral cell lateral dendrites in a dendritic meshwork structure of the developing mouse olfactory bulb. J. Comp. Neurol. *523*, 1824–1839. https://doi.org/10.1002/cne.23762.

45. Mizutani, K., and Takai, Y. (2016). Nectin spot: a novel type of nectin-mediated cell adhesion apparatus. Biochem. J. *473*, 2691–2715. https://doi.org/10.1042/BCJ20160235.
46. Li, Y., Xu, B., Jin, M., Zhang, H., Ren, N., Hu, J., and He, J. (2023). Homophilic interaction of cell adhesion molecule 3 coordinates retina neuroepithelial cell proliferation. J. Cell Biol. *222*, e202204098. https://doi.org/10.1083/jcb.202204098.
47. Wang, Y.V., Weick, M., and Demb, J.B. (2011). Spectral and temporal sensitivity of cone-mediated responses in mouse retinal ganglion cells. J. Neurosci. *31*, 7670–7681. https://doi.org/10.1523/JNEUROSCI.0629-11.2011.
48. Takai, Y., Ikeda, W., Ogita, H., and Rikitake, Y. (2008). The immunoglobulin-like cell adhesion molecule nectin and its associated protein afadin. Annu. Rev. Cell Dev. Biol. *24*, 309–342. https://doi.org/10.1146/annurev.cellbio.24.110707.175339.
49. Zhou, Y., Du, G., Hu, X., Yu, S., Liu, Y., Xu, Y., Huang, X., Liu, J., Yin, B., Fan, M., et al. (2005). Nectin-like molecule 1 is a protein 4.1N associated protein and recruits protein 4.1N from cytoplasm to the plasma membrane. Biochim. Biophys. Acta *1669*, 142–154. https://doi.org/10.1016/j.bbamem.2005.01.013.
50. Shen, L., Liang, F., Walensky, L.D., and Huganir, R.L. (2000). Regulation of AMPA receptor GluR1 subunit surface expression by a 4. 1N-linked actin cytoskeletal association. J. Neurosci. *20*, 7932–7940. https://doi.org/10.1523/JNEUROSCI.20-21-07932.2000.
51. Sanuki, R., Watanabe, S., Sugita, Y., Irie, S., Kozuka, T., Shimada, M., Ueno, S., Usukura, J., and Furukawa, T. (2015). Protein-4.1G-mediated membrane trafficking is essential for correct rod synaptic location in the retina and for normal visual function. Cell Rep. *10*, 796–808. https://doi.org/10.1016/j.celrep.2015.01.005.
52. Kemmler, R., Schultz, K., Dedek, K., Euler, T., and Schubert, T. (2014). Differential regulation of cone calcium signals by different horizontal cell feedback mechanisms in the mouse retina. J. Neurosci. *34*, 11826–11843. https://doi.org/10.1523/JNEUROSCI.0272-14.2014.
53. Poché, R.A., Kwan, K.M., Raven, M.A., Furuta, Y., Reese, B.E., and Behringer, R.R. (2007). Lim1 is essential for the correct laminar positioning of retinal horizontal cells. J. Neurosci. *27*, 14099–14107. https://doi.org/10.1523/JNEUROSCI.4046-07.2007.
54. Reese, B.E., Raven, M.A., and Stagg, S.B. (2005). Afferents and homotypic neighbors regulate horizontal cell morphology, connectivity, and retinal coverage. J. Neurosci. *25*, 2167–2175. https://doi.org/10.1523/JNEUROSCI.4876-04.2005.
55. Poché, R.A., Raven, M.A., Kwan, K.M., Furuta, Y., Behringer, R.R., and Reese, B.E. (2008). Somal positioning and dendritic growth of horizontal cells are regulated by interactions with homotypic neighbors. Eur. J. Neurosci. *27*, 1607–1614. https://doi.org/10.1111/j.1460-9568.2008.06132.x.
56. Mouland, J.W., Pienaar, A., Williams, C., Watson, A.J., Lucas, R.J., and Brown, T.M. (2021). Extensive cone-dependent spectral opponency within a discrete zone of the lateral geniculate nucleus supporting mouse color vision. Curr. Biol. *31*, 3391–3400.e4. https://doi.org/10.1016/j.cub.2021.05.024.
57. Ye, Y., Dinh Duong, T.A., Saito, K., Shinmyo, Y., Ichikawa, Y., Higashide, T., Kagami, K., Fujiwara, H., Sugiyama, K., and Kawasaki, H. (2020). Visualization of the retina in intact eyes of mice and ferrets using a tissue clearing method. Transl. Vis. Sci. Technol. *9*, 1. https://doi.org/10.1167/tvst.9.3.1.
58. Lei, B. (2012). Rod-driven OFF pathway responses in the distal retina: dark-adapted flicker electroretinogram in mouse. PLoS One *7*, e43856. https://doi.org/10.1371/journal.pone.0043856.
59. Shirato, S., Maeda, H., Miura, G., and Frishman, L.J. (2008). Postreceptoral contributions to the light-adapted ERG of mice lacking b-waves. Exp. Eye Res. *86*, 914–928. https://doi.org/10.1016/j.exer.2008.03.008.
60. Sugita, Y., Araki, F., Chaya, T., Kawano, K., Furukawa, T., and Miura, K. (2015). Role of the mouse retinal photoreceptor ribbon synapse in visual motion processing for optokinetic responses. PLoS One *10*, e0124132. https://doi.org/10.1371/journal.pone.0124132.
61. Watanabe, S., Sanuki, R., Sugita, Y., Imai, W., Yamazaki, R., Kozuka, T., Ohsuga, M., and Furukawa, T. (2015). Prdm13 regulates subtype specification of retinal amacrine interneurons and modulates visual sensitivity. J. Neurosci. *35*, 8004–8020. https://doi.org/10.1523/JNEUROSCI.0089-15.2015.

STAR★METHODS

KEY RESOURCES TABLE

REAGENT or RESOURCE	SOURCE	IDENTIFIER
Antibodies		
Rabbit polyclonal anti-Necl-1	Kobe University	N/A Kakunaga et al.[26]
Mouse Anti-CtBP2	BD Biosciences	Cat# 612044; RRID: AB_399431
Goat polyclonal anti-OPN1SW	Santa Cruz	Cat# sc-14363; RRID: AB_2158332
Rabbit polyclonal anti-Opsin Antibody, Red/Green	Millipore	Cat# AB5405; RRID: AB_177456
Mouse monoclonal anti-rhodopsin, RET-P1 (RHO)	Sigma-Aldrich	Cat# O4886; RRID: AB_260838
Mouse monoclonal anti-HCN4	Sigma-Aldrich	Cat# SAB5200035; RRID: AB_3095881
Mouse monoclonal anti-PKARIIβ	BD Biosciences	Cat# 610625; RRID: AB_397957
Mouse monoclonal anti-calsenilin	Millipore	Cat# 05–756; RRID: AB_309969
Mouse monoclonal anti-SYT2	Abcam	Cat# ab154035; RRID: AB_2916272
Mouse monoclonal anti-PKCα	Santa Cruz	Cat# sc-8393; RRID: AB_628142
Mouse monoclonal anti-calbindin	Sigma-Aldrich	Cat# C9848; RRID: AB_476894
Rabbit polyclonal anti-calbindin	Millipore	Cat# AB1778; RRID: AB_2068336
Mouse monoclonal anti-GluR5 (GluK1)	Santa Cruz Biotechnology	Cat# sc-393420; RRID: AB_2716684
Mouse monoclonal anti-GluR1 (GluA1)	Abcam	Cat# ab31232; RRID: AB_2113447
Alexa Fluor 594-conjugated lectin peanut agglutinin (PNA)	Vector Laboratories	Cat# RL-1072; RRID: AB_2336642
Goat polyclonal anti-Chx10	Santa Cruz	Cat# sc-21690; RRID: AB_2216006
Rabbit polyclonal anti-β-actin	Proteintech Group	Cat# 20536-1-AP; RRID: AB_10700003
Alexa Fluor 488 goat anti-rabbit	Jackson Immunoresearch Laboratories	Cat# 111-585-144; RRID: AB_2307325
Alexa Fluor 594 goat anti-mouse	Jackson Immunoresearch Laboratories	Cat# 115-585-146; RRID: AB_2338881
Alexa Fluor 555 goat anti-guinea pig	Thermo Fisher Scientific	Cat# A-21435; RRID: AB_2535856
Goat anti-rabbit IgG H&L (HRP)	Abcam	Cat# ab6721; RRID: AB_955447
Chemicals, peptides, and recombinant proteins		
cis-2,3-piperidinedicarboxylic acid	Abcam	Cat# ab120038
L-2-amino-4-phosphobutyric acid	Sigma-Aldrich	Cat# A212
LY404187	Tocris Bioscience	Cat# No. 5297

(*Continued on next page*)

Continued

REAGENT or RESOURCE	SOURCE	IDENTIFIER
Critical commercial assays		
REDExtract-N-Amp™ Tissue PCR Kit	Sigma-Aldrich	Cat# No. 254-457-8
Gel Extraction Kit	Thermo Fisher Scientific	Cat# No. K0691
Zero Blunt TOPO PCR Cloning Kit	Thermo Fisher Scientific	Cat# No. 451245
Chemi-Lumi One L assay kit	Nacalai Tesque	Cat# No. 07880-54
Deposited data		
Single-cell RNA-seq data in retinal bipolar cells	Shekhar et al.[22]	GEO: GSE81905
Experimental models: Organisms/strains		
Mouse: B6.129/Sv RW4- *Necl-1/J*	This paper	N/A
Oligonucleotides		
Primers for genotyping Forward: ACACTACCACACTTCCTCCTT	This paper	N/A
Primers for genotyping Reverse: TTTCCCGCAATGATGACTTAT	This paper	N/A
Primers for genotyping Forward: CTGACCGCTTCCTCGTGCTTT	This paper	N/A
Primers for genotyping Reverse: TTTGTCTGTGGCTGCTCTCCT	This paper	N/A
Primers for Necl-1 cDNA Forward: AAAATGGGGCAGCTGCAAT	This paper	N/A
Primers for Necl-1 cDNA Reverse: AGTCGGGTGGCATGCTTTAA	This paper	N/A
Software and algorithms		
Powerlab	ADI Instruments	https://www.adinstruments.co.jp/products
LabChart	ADI Instruments	https://www.adinstruments.co.jp/products
Origin 9.1	LightStone	N/A
Pyclesperanto	Python Software Foundation	https://pypi.org/project/pyclesperanto/
3D Voronoi-Otsu-Labeling, Voronoi diagram	This paper	N/A
Single Cell Portal	This paper	RRID:SCR_014816
Other		
NSHU551B	Nichia	Cat# No. 131107
TQ 8210	Advantest	Cat# No. 71027-3
NSPW310BS	Nichia	Cat# No. 031110
U-330	HOYA	N/A

RESOURCE AVAILABILITY

Lead contact

Further information and requests for resources and reagents should be directed to Kenji Matsushita (kenmatsu@ophthal.med.osaka-u.ac.jp).

Materials availability

- The Necl-1 knockout mouse line used in this study was generated by Jun Miyoshi. Kenji Mandai and Rumi Kawashima bred and managed mice.
- The Necl-1 antibody used in this study was generated by Yoshimi Takai.[26]

Data and code availability

- All datasets reported in this study can be shared by the lead contact upon request.
- Single-cell RNA-seq data in retinal bipolar cells have been deposited at GEO: GSE81905 and are publicly available as of the date of publication.
- Any additional information required to reanalyze the data reported in this study is available from the lead contact upon request.
- This paper does not report original code.

EXPERIMENTAL MODEL AND STUDY PARTICIPANT DETAILS

Mice

All animal experiments other than developmental experiment were performed using C57BL/6J mice (Japan SLC, Hamamatsu, Japan), *Necl-1*$^{-/-}$ mice, and their WT littermates at 8 weeks of age (8-week groups). In Figure S3, postnatal 2-, 7-, 14-, and 21-day-old mice were used, and in Figure S7, postnatal 4-, 6-day-old mice were used. We used male and female mice in the histological experiments, and in physiological experiments, we used male mice to eliminate the estrus cycle. Mice were housed in a temperature-controlled room at 23 ± 1.5 °C at Osaka University with a 12:12 h light-dark cycle (light on at 8:00 AM and off at 8:00 PM; ambient temperature, 23 ± 1.5°C; relative humidity, 45 ± 15%). Fresh water and standard certified rodent diet (MF; Oriental Yeast Company, Osaka, Japan) were always available. All procedures conformed to the Association for Research in Vision and Ophthalmology Statement for the Use of Animals in Ophthalmic and Vision Research were approved by the Institutional Animal Care and Use Committee (approval ID 26-034-009) and performed according to Animal Experiment guidelines of Osaka University.

Generation of Necl-1$^{-/-}$ mice

To replace the *Necl-1* genomic region between the SacI site in exon 3 and the SmaI site in exon 5 with an *MC1* promoter-Neo-poly A cassette, a targeting vector was constructed using a 5.6-kb SacI fragment (from the SacI site in intron 1 to the SacI site in exon 3) and a 3.9-kb SmaI-HpaI fragment (from the SmaI site in exon 5 to the HpaI site in intron 7) (Figure S1D). The *MC1* promoter-diphtheria toxin A fragment-poly A cassette was used for negative selection. The targeted region contained amino acids 90–198 of the Necl-1 protein. The linearized targeting vector was transfected into 129/Sv RW4 embryonic stem (ES) cells (Genome Systems, St. Louis, MO) by electroporation. ES cells harboring the targeted allele were selected for G418 resistance and then microinjected into C57BL/6 blastocysts to obtain chimeric mice. Chimeric mice were bred with BDF1 mice to generate heterozygous mice carrying the mutant allele. Mice were genotyped by PCR using DNAs from tail biopsies. Primer sequences for genotyping were as follows: F1, 5′-ACACTACCACACTTCCTCCTT-3′; R1, 5′-TTTCCCGCAATGATGACTTAT-3′; F2, 5′-CTGACCGCTTCCTCGTGCTTT-3′; and R2, 5′-TTTGTCTGTGGCTGCTCTCCT-3′. The PCR protocol consisted of 2 min at 95°C followed by 35 cycles of 30 s at 95°C, 30 s at 57°C, and 30 s at 72°C. Primer pair F1 and R1 gave a 271-bp band for a WT allele, while primer pair F2 and R2 gave a 485-bp band for a mutant allele. *Necl-1*$^{+/-}$ mice that were used to produce *Necl-1*$^{-/-}$ mice had been backcrossed with C57BL/6J mice for more than 10 generations.

METHOD DETAILS

In situ hybridization

Total RNA was isolated from mouse brain and complementary DNAs were generated from 1 μg of total RNA. Mouse *Necl-1* cDNA was amplified using primers: 5′-AAAATGGGGCAGCTGCAAT-3′, and 5′-AGTCGGGTGGCATGCTTTAA-3′. PCR products were purified with a Gel Extraction Kit (Thermo Fisher Scientific, Waltham, MA) and cloned using the Zero Blunt TOPO PCR Cloning Kit (Thermo Fisher Scientific). Cloned cDNA was confirmed by sequencing. To prepare sense and antisense probes, template DNAs were linearized by digesting them with NotI and SpeI, respectively. RNA probes were prepared using the following reaction mixture and labeled with digoxigenin: 1-μg linearized DNA; diethylpyrocarbonate (DEPC)-treated distilled water to a total volume of 20 μL; 4 μL 5× transcription buffer; 2 μL 10× DIG-RNA labeling mix; 1 μL RNase inhibitor; 2 μL T3 RNA polymerase. For hybridization, eyes were enucleated and freshly frozen in cryo-embedding medium. Retinas were cut into 18-μm sections with a cryostat and fixed with 4% formaldehyde for 19 min at room temperature, followed by three washes with DEPC-treated PBS, and DEPC-treated distilled water. Sections were acetylated for 10 min at room temperature in the presence of 1% triethanolamine and 0.25% acetic anhydride, and then washed in DEPC-treated PBS. Slides were prehybridized for 1 h at 65°C in hybridization solution containing: 50% formamide; 5× SSC; 0.3 mg/mL Baker's yeast tRNA; 0.1 mg/mL heparin; 1× Denhardt's solution; 0.1% Tween 20; 0.1% CHAPS; and 5 mM EDTA. Probes were prepared at a concentration of 200 ng in 150 μL hybridization solution, and slides with probe solution were covered with PCR film and hybridized overnight at 65°C in a humidified chamber. After hybridization, sections were washed three times with 20× SSC at 65°C. Sections were washed in 0.1% Triton X-100 in PBS, blocked with 20% normal goat serum in 0.1% Triton X-100 in PBS for 1 h at room temperature, and incubated with an anti-DIG-Fab (1:2,000) in 20% normal goat serum and 0.1% Triton X-100 in PBS in a humidified chamber overnight at 4°C. After three washes with 0.1% Triton X-100 in PBS, and immersion for 5 min in a solution containing 100 mM Tris-HCl (pH 9.5), 100 mM NaCl, and 5 mM $MgCl_2$, sections were incubated with a developing solution containing 0.3375 mg/mL 4-nitro blue tetrazolium chloride, 0.165 mg/mL 5-bromo-4-chloro-3-indolyl-phosphate, and 0.24 mg/mL levamisole for 45 min at room temperature. They were then immersed in 5 mM EDTA in PBS for 10 min to stop the color reaction.

Antibodies

The rabbit anti-Necl-1 pAb (used at a 1:300 dilution for immunohistochemistry and Western blots) was used.[26] The following antibodies used in this study were purchased from commercial sources: mouse anti-CtBP2 mAb (1:200) (BD Biosciences, San Jose, CA); goat anti-OPN1SW (S-opsin) pAb (1:500) (Santa Cruz Biotechnology, Dallas, TX); rabbit anti-red-green (L/M) opsin pAb (1:200) (Millipore, Burlington, MA); mouse anti-rhodopsin, RET-P1 (RHO) mAb (1:10,000) (Sigma-Aldrich Japan, Tokyo, Japan); mouse anti-HCN4 mAb (1:200) (Sigma-Aldrich Japan); mouse anti-PKARIIβ mAb (1:200) (BD Biosciences, San Jose, CA); mouse anti-SYT2 mAb (1:200) (Abcam, Cambridge, UK); mouse anti-calsenilin mAb (1:200) (Millipore); mouse anti-PKCα mAb (1:200) (Santa Cruz Biotechnology); mouse anti-calbindin mAb (1:3,000) (Sigma-Aldrich Japan); rabbit anti-calbindin pAb (1:2,000) (Millipore); mouse anti-GluR5 (GluK1) mAb (1:100) (Santa Cruz Biotechnology); rabbit anti-GluR1 (GluA1) pAb (1:200) (Abcam, Cambridge, UK); Alexa Fluor 594-conjugated lectin peanut agglutinin (PNA) (1:200) (Vector Laboratories, Burlingame, CA); anti-Chx10 pAb (1:200) (Santa Cruz Biotechnology); and rabbit anti-β-actin pAb (1:1,000) (Cosmo Bio, Tokyo, Japan). Alexa Fluor 488 goat anti-rabbit Ab, 594 goat anti-mouse Ab (1:300) (Jackson Immunoresearch Laboratories, West Grove, PA), and Alexa Fluor 555 goat anti-guinea pig Ab (1:500) (Thermo Fisher Scientific) were used as secondary Abs.

Western blot analysis

Mouse eyes were enucleated and their corneas, lenses, choroids, and sclerae were removed. Mouse retinas were homogenized in RIPA lysis buffer (Cosmo Bio) and protein extracts were prepared using NuPAGE LDS Sample Buffer (Thermo Fisher Scientific). Forty micrograms of protein per lane were loaded onto NuPAGE Novex 4–12% Bis-Tris Gels (Thermo Fisher Scientific), separated, and then transferred to an iBlot Transfer Stack, Regular polyvinylidene difluoride membranes (Thermo Fisher Scientific) using the iBlot Gel Transfer Device (Thermo Fisher Scientific). Membranes were blocked with Blocking One blocking buffer (Nacalai Tesque, Kyoto, Japan) at 4°C overnight, and washed five times for 5 min in Tris-buffered saline plus 0.05% Tween 20. Membranes were then incubated with the Ab indicated for each experiment in blocking buffer at 4°C overnight. After washing with Tris-buffered saline plus 0.05% Tween 20, membranes were incubated with goat anti-rabbit IgG H&L (HRP) Ab (1:1,000; Abcam) in blocking buffer at 4°C overnight. Protein bands were detected using a Chemi-Lumi One L assay kit (Nacalai Tesque).

Immunohistochemistry

For immunohistochemical staining of tissue sections, enucleated eyes were fixed in 4% PFA at 4°C for 2 h, washed in PBS, and immersed in 30% sucrose in PBS until they sank. Then, eyes were embedded in OCT compound, frozen, and stored at −80°C. Frozen sections were cut at 10 μm and mounted on glass slides. Sections were washed three times in 0.05% saponin in PBS, blocked at room temperature for 30 min in 20% Block Ace (Megmilk Snow Brand, Sapporo, Japan) and 0.05% saponin in PBS, and incubated with the indicated primary Ab in 5% Block Ace and 0.05% saponin in PBS at 4°C overnight. Slides were washed with 0.05% saponin in PBS three times and incubated with secondary Abs in 5% Block Ace and 0.05% saponin in PBS at room temperature for 1 h. Sections were washed in 0.05% saponin in PBS and mounted in PermaFluor Aqueous Mounting Medium (Thermo Fisher Scientific).

For whole-mount immunostaining, eyes were briefly fixed were in 4% PFA and methanol at 4°C, washed in PBS. Retinas were isolated from eyeballs and blocked at 4°C for 2 h in PBS containing 0.1% Triton X-100, 2% Skim milk, 1% goat serum (GS), and 0.2% bovine serum albumin (BSA), and incubated with the indicated primary Ab in blocking buffer at 4°C overnight. Retinal whole-mounts were washed and incubated with secondary Abs in blocking buffer at 4°C overnight. Retinas were washed and mounted in PermaFluor Aqueous Mounting Medium. Confocal images were acquired with an LSM710 confocal laser-scanning microscope system (Carl Zeiss Microscopy, Cambridge, UK) using a Zeiss EC Plan-Neofluar 40×/1.3 NA oil or 60×/1.4 NA oil immersion objective lens. High-resolution immunofluorescence microscopy was performed with a DeltaVision Elite microscope system (GE Healthcare, Buckinghamshire, UK) fitted with an Olympus U-Plan S-Apo 60×/1.42 NA oil or 100×/1.4 NA oil objective lens.

Retinal whole-mount analysis

We performed tissue clearing to visualize distribution patterns and morphology of Necl-1-positive bipolar cells. We prepared flat-mounted retinas using a modification of the method of Ye et al.[57] In brief, after being fixed in 4% PFA and methanol, retinas marked on the dorsal side were isolated and immersed in CUBIC-L (Tokyo Chemical Industry Co., Ltd., Tokyo, Japan) at room temperature for one day with gentle shaking. After immunostaining using the methods described above, retinas were immersed in CUBIC-R (Tokyo Chemical Industry Co., Ltd., Tokyo, Japan) at room temperature for 1 day. Retinas were mounted on slides and images of retinas were taken using an LSM710 confocal laser-scanning microscope system (Carl Zeiss Microscopy, Cambridge, UK). Acquired images were analyzed using the original workflow with py-clesperanto, a python wrapper library for GPU-accelerated image processing. Separate RGB images from original image data to acquire the nuclear staining signal (Red) and the Necl-1 staining signal (Green). First, we homogenized images using the following preprocessing steps: local contrast correction, intensity correction to keep the maximum brightness per retina slice, and background component removal. Next, we extracted each nucleus in the red signal image using the 3D Voronoi-Otsu-Labeling approach. Specifically, we detected the strongest point of the red signal, and from that point, image expansion processing was performed to make the image recognize individual nuclei when it was expanded until the signal intensity disappeared. Then, we separated individual nuclei using a Voronoi diagram to extract nuclei from the image in three dimensions, giving colors to each nucleus at random. If this image was further expanded and programmed to retain only those nuclei recognized as Green, Necl-1-positive bipolar cells can be identified among all nucleus-stained bipolar cells

(Figures S2B and S2C). This method was followed by cell counting using proprietary software to determine the percentage of Necl-1-positive cells among retinal bipolar cells. This process was performed on prepared acquired images and the dorsoventral distribution was calculated. Numbers of samples are presented in the Quantification and statical analysis section of each method.

ERG recording

ERGs were recorded according to the protocol of the International Society of Clinical Electrophysiology of Vision (ISCEV). Briefly, animals were dark-adapted for scotopic responses over 16 h and anesthetized with ketamine (70 mg/kg) and xylazine (14 mg/kg). Pupils were dilated with tropicamide and phenylephrine hydrochloride (Santen Pharmaceutical, Osaka, Japan), and corneal surfaces were protected with scopisol solution (Senju Pharmaceutical, Osaka, Japan). ERGs were evoked with LED-generated light flashes using a stimulator (WLS-20) (Mayo, Inazawa, Japan). A needle electrode was applied to the middle of the forehead as a reference and a clip electrode was connected to the tail as a ground electrode. Recording was performed for about 1 h using a heating pad. Signals were amplified and band-pass filtered between 0.5–300 Hz using a memory oscilloscope (VC-11; Nihon Kohden, Tokyo, Japan). Results were transferred to Powerlab (ADI Instruments, Nagoya, Japan) and analyzed using Labchart (ADI Instruments, Nagoya, Japan) and Origin 9.1 softwares (LightStone, Tokyo, Japan).

UV-elicited electroretinography

ERGs were recorded using a UV-LED (NSHU551B; λmax = 365 nm, half-width = 12 nm; Nichia, Anan, Japan) light stimulator (Mayo) in a custom-made, aluminum-framed cage, the interior of which was shaded from light. The light stimulator was adjusted to deliver the light 2 cm above the cornea, parallel to the optic axis. Light intensity was measured with an optical power meter (TQ 8210; Advantest, Tokyo, Japan). Without dark adaptation, photopic single-flash ERGs were recorded at 17-sec intervals with a light intensity of 5.49 $\mu W \cdot sec/cm^2$. Photopic flicker ERG responses were obtained at varying frequencies (5, 10, 12.5, 15, 25, and 30 Hz) at a fixed luminance (202.8 $\mu W \cdot ms/cm^2$) and averaged over many trials.

The light signal was first separated into ON and OFF pathways at the first synapse in the OPL. However, the long duration ERG protocol used in primates to detect OFF responses is not applicable to mice, because the OFF response is extremely weak in mouse retina. Therefore, Tanimoto et al. tried to separate the OFF reaction utilizing the fact that the ON reaction is attenuated at high frequencies.[28] By reducing recording noise sufficiently, separation became possible. Kawashima et al further applied this method to UV-induced ERGs and succeeded.[29] We used this method in the present study.

PDA was used as a non-specific ionotropic GluR inhibitor in the present study. Kawashima et al used a high concentration of PDA (26.3 mM), with which the recording ERG amplitude at 30 Hz decreases to below the noise level.[29] On the other hand, in the present study, we analyzed latency using PDA at 13.15 mM, keeping the amplitude above the noise level. When 400 μM NBQX (more selective AMPA receptor antagonist than CNQX, 1044, Tocris Bioscience, Bristol, UK) was used, the ERG amplitude at 30 Hz decreased and latency was extended. These results suggested that the AMPA signal pathway via ionotropic GluRs was mainly responsible for the OFF response.

Intravitreal drug administration

Intravitreal injection was performed as previously described.[29,58,59] Briefly, a small hole was made in the eye with a 30-gauge needle at a position 500 μm posterior to the limbus, and 1.5 μL of solution were injected into the eye through a glass pipette needle attached to a Hamilton syringe (GL Science, Tokyo, Japan). Injections of the following were performed: NMDA, AMPA, and KA receptor antagonists, PDA (Abcam); the mGluR6 receptor agonist, L-AP4 (Sigma-Aldrich, St. Louis, MO); the AMPA receptor potentiator, LY404187 (Tocris Bioscience); and saline, as a control. Vitreal concentrations of PDA and LY404187 were calculated as 13.15 mM and 10 μM, respectively, by estimating the vitreous volume at approximately 6.6 μL. Responses were observed from 15 min to 1 h after solution injection. Photopic 30-Hz flicker ERG responses were obtained at a fixed luminance (202.8 $\mu W \cdot ms/cm^2$) and averaged over many trials. ERGs elicited by short-duration flashes (2 ms) at a fixed luminance (959.4 $\mu W \cdot ms/cm^2$) and long-duration flashes (100–300 ms) at a fixed luminance (31.3 $\mu W \cdot ms/cm^2$) were recorded after injection of L-AP4.

White LED-elicited electroretinography

ERGs were detected with an electrode embedded in a contact lens electrode (NSPW310BS; Nichia). For scotopic responses, ERGs were averaged from five flashes with a 30 s interstimulus period for each of the following light intensities: -2, 0.5, 1, 1.5 log $cd \cdot s/m^2$. For photopic responses, after light adaptation for 15 min, single-flash ERGs at light intensities of 0.5, 1, 1.5 log $cd \cdot s/m^2$, and flicker ERGs at a fixed luminance (0.5 log $cd \cdot s/m^2$) were recorded, with a background luminance of 25 cd/m^2. A-wave and b-wave amplitudes and latency were measured after oscillatory potentials were removed. Oscillatory potentials were extracted after filtering full-flash ERG recordings between 75–300 Hz, and amplitudes of five peaks (OP1–OP5) were automatically analyzed using Origin 9.1 software (LightStone).

OKR recording

Animal preparation, OKR recording, and visual stimulation were performed as previously described.[37,38,60,61] The initial phase of the OKR (~500 ms from the onset of visual stimulus motion) was examined. In brief, right eye movement was monitored using a video-based eye-tracker system (Geteye; Matsuura-Denko-sha, Nonoichi, Japan). Visual stimuli were vertical sinusoidal gratings with a sinusoidally-modulated luminance. Spatial frequency, temporal frequency, and mean luminance were set at 0.125 cycle/deg, 1.5 Hz, and 100 cd/m^2, respectively. At

the beginning of each trial, the grating was stationary for 333 ms and then moved either counterclockwise or clockwise at a constant speed. After a defined period, the grating was removed.

To study the dependence of eye movement on the short-wavelength region of visual stimuli, the same experiment was performed with only short-wavelength stimuli using UV bandpass filters (U-330; HOYA, Tokyo, Japan). The UV bandpass filter transmits short-wavelength light (200–400 nm; central wavelength, 330 nm), but reflects visible light, such that mice can see only short-wavelength light from visual stimuli.[29]

Single-cell RNA-seq data Sub analysis

We acquired single-cell RNA-seq data in the Study: Retinal Bipolar Neuron Drop-seq from the Single-cell portal website provided by the Broad Institute (Cambridge, MA, USA).[22] We analyzed those data with the analytical software, Single Cell Portal beta. It made a violin plot of gene expression of cadm3 coding Necl-1 in bipolar cells and other retinal neurons. The code for this integration and scRNA-seq reanalysis can be obtained from the following Repository:

https://singlecell.broadinstitute.org/single_cell/study/SCP3/retinal-bipolar-neuron-drop-seq.

QUANTIFICATION AND STATISTICAL ANALYSIS

All experiments were performed with WT and *Necl-1*$^{-/-}$ littermates. In Figure 1I, we analyzed the Necl-1 signal detected in strata 1, 2, 3, and 4/5 of IPL using software of the DeltaVision Elite microscope system (GE Healthcare, Buckinghamshire, UK) in WT mice (n=4). In Figure 2E, we analyzed the percentage of Necl-1-positive cells among photoreceptors in n = 6 to 8 retina sections per WT mouse (n = 3). In Figures 4B–4D, 4F, 4I, and 4L, we counted the number of marker-positive cells in n = 5 to 9 retina sections from individual animals (n = 4 and 5; WT and *Necl-1*$^{-/-}$, respectively). In Figures 4G–4J, and 4M, we counted the number of bipolar dendrites with aberrant sprouting synaptic terminals into the ONL in n = 5 to 8 retina sections from individual animals (n = 4 and 5; WT and *Necl-1*$^{-/-}$, respectively). We analyzed photopic flicker and long-flash ERGs (n = 7 in Figures 5B and 5C; WT and *Necl-1*$^{-/-}$, respectively, n = 4 and 5 in Figures 5E and 5F; WT and *Necl-1*$^{-/-}$, respectively, n = 6 in Figures 7B and 7C; WT saline, WT PDA, and, n = 6, 5, 6, and 4 in Figures 7E and 7F; *Necl-1*$^{-/-}$saline, *Necl-1*$^{-/-}$ LY404187, WT saline, and WT LY404187, respectively). In Figure 6C, we analyzed abnormal localization of GluA1 in OPL. We calculated the percentage of GluA1 at inner sides of cone pedicles (PNA) (n = 5; WT and *Necl-1*$^{-/-}$, respectively). In Figure 8B, we measured the distance between somata of calbindin-positive HC cells and the OPL in n = 36 HCs from individual animals (n = 4; WT and *Necl-1*$^{-/-}$, respectively). In Figure 8C, we counted the number of calbindin-positive cells in n = 6 to 11 retina sections from individual animals (n = 3 and 4; WT and *Necl-1*$^{-/-}$, respectively). In Figures 8E and 8G, we analyzed the percentage of HCs surrounded by BCs, because the HC located at a more inner position in the ONL is surrounded by BCs (n = 36 HCs from individual animals (n = 3; WT and *Necl-1*$^{-/-}$, respectively)). In the immunohistological analysis, we randomly selected the retina section. We blindly analyzed OKR in Figures 9F and 9G (n = 6 and 5; WT and *Necl-1*$^{-/-}$, respectively). In whole-mount analysis in Figure S2, we selected each 2-3 parts of dorsal and ventral retina (n=4) and blindly analyzed the percentage of Necl-1-positive bipolar cells. Statistical analysis of the difference between two means was performed with two-tailed, paired Student's *t* tests in Figures 4, 5, and 6, 7B, 7C, and 9 or by Wilcoxon signed-rank tests in Figures 7E and 7F. We applied t-tests to samples with normal distributions or large number of specimens and Wilcoxon tests to samples with non-normal distributions. The criterion for statistical significance was $p < 0.05$.